Recent developments in high-performance thermoelectric sulphides: an overview of the promising synthetic colusites

Gabin Guelou, Pierric Lemoine, Bernard Raveau, Emmanuel Guilmeau

Review paper

Recent developments in high-performance thermoelectric sulphides: an overview of the promising synthetic colusites

Gabin Guélou,[a,*] Pierric Lemoine,[b] Bernard Raveau,[a] Emmanuel Guilmeau [a,*]

[a] CRISMAT, CNRS, Normandie Univ, ENSICAEN, UNICAEN, 14000 Caen, France

[b] ISCR – UMR 6226, CNRS, Univ Rennes, F-35000 Rennes, France

* Corresponding authors: gabin.guelou@live.fr
emmanuel.guilmeau@ensicaen.fr

Abstract

Derivatives of the natural mineral colusite with general formula $Cu_{26}A_2E_6S_{32}$ (*A* = V, Nb, Ta, Cr, Mo, W; *E* = Ge, Sn, As, Sb), are an emerging class of excellent thermoelectric materials. Within just a few years, they have been promoted as serious candidates for cost-efficient, environmentally-friendly thermoelectric power generation, reaching performances comparable to tetrahedrites and other advanced thermoelectric sulphides. From ultralow thermal conductivity to record-high power factor, this review gives an extensive description of the current state of the art regarding the crystal chemistry and electrical and thermal transport properties of colusites.

Table of contents

1. Introduction

Thermoelectricity is an old concept that began more than 2 centuries ago with the combined discoveries of Aloisio Galvani, Alessandro Volta, Thomas Johann Seebeck, Hans Christian Ørsted, Jean Baptiste Joseph Fourier, Jean Charles Athanase Peltier and later William Thomson, among many others. While the historical aspect of thermoelectricity falls outside the scope of this review, we strongly encourage researchers to read the excellent and very extensive work of Beretta *et al.*, that includes a fascinating read about the history of thermoelectricity.[1] Since this early start, thermoelectricity has evolved to become a new potential source of renewable electricity, as well as a novel and versatile technology for heating and cooling devices.[2,3] Thermoelectric devices can thus be used as green energy power generators by converting a temperature difference into a useful electrical current. This configuration is particularly attractive considering the challenges that we are facing as a result of our reliance on industrial processes with high-levels of greenhouse gas emissions. Alternatively, thermoelectric devices can also be used as reliable, long-lived heaters or coolers for specific applications where traditional systems fail to meet special requirements such as the absence of mobile parts and vibrations.

In any case, in order to become a more popular technology, thermoelectric devices must simultaneously improve their rather limited efficiency and decrease the cost of raw materials. This is particularly true for power generation as a large-scale implementation of cost-efficient devices is necessary to have a meaningful impact in the race against climate change. The efficiency of a thermoelectric module depends in part on the performance of its component *n*-type and *p*-type materials. This performance is usually demonstrated by a high value of the dimensionless figure-of-merit, *ZT*, expressed as:

$$ZT = \frac{S^2\sigma}{\kappa}T$$

where *S* is the Seebeck coefficient, σ is the electrical conductivity, κ is the total thermal conductivity and *T* is the temperature. The maximum efficiency of the device, ignoring contact resistance, can then be estimated using the equation:

$$\eta_{max} = \frac{\Delta T}{T_{hot}} \frac{\sqrt{1+ZT_{avg}}-1}{\sqrt{1+ZT_{avg}}+\frac{T_{cold}}{T_{hot}}}$$

where $\Delta T/T_{hot}$ is the Carnot efficiency and ZT_{avg} is the averaged ZT between the component *n*-type and *p*-type materials. For comparison purposes, the current commercialised thermoelectric devices have an efficiency of less than 10 % achieved with figure of merits around 1.[4,5] In term of materials,

current state-of-the-art thermoelectric modules, in particular for mid-range temperatures (400 < T / K < 600), are often composed of materials prepared from heavy, toxic, rare and/or expensive elements such as Ag, Bi, Pb, Se, Te, etc. ([2,6] and references therein)

Indeed, the sustainability being at the heart of the concept of wide-scale thermoelectric modules for energy recovery, it is crucial that the materials within these modules are not only cheap, but abundant and easy to synthesise. Naturally, selenides and tellurides, while offering excellent thermoelectric performances, fall outside of the category of sustainable materials. With an overall abundance of 4 to 5 orders of magnitude greater than Se or Te, sulphur is a much more desirable substitute.[7] The availability of tellurium has been deemed critical by the U.S. government, where the production of thermoelectric devices already accounts for 30% of the global consumption of Te, only slightly behind the solar industry at 40%.[8] It is clear that tellurides are not suitable materials for a cost-effective, truly sustainable, wide-scale thermoelectric power recovery. Selenium does not seem to be a much better alternative with a terrestrial abundance of only 50 ppb, against 3.5×10^5 ppb for sulphur. A very detailed comparison between the three chalcogens has been proposed by Powell, including cost, toxicity and availability constraints.[7]

The past few years have seen a renewed interest for thermoelectric sulphides as the earth-abundance of sulphur is one critical aspect to encourage the large-scale production of devices with a potentially meaningful impact on mitigating climate change.[7] Researchers have also suggested using natural mineral as a direct source of thermoelectric, such as chalcopyrite or tetrahedrite,[9–11] although better performances are usually achieved for a synthetic derivative.[12–21] Over the last decade, following reports of excellent properties in ternary and quaternary sulphides, the performance of cost-efficient sulphides have gotten closer to that of well-established state-of-the-art materials such as chalcogenides,[22–24] oxy-chalcogenides,[22,25–27] clathrates,[28,29] skutterudites,[30,31] Zintl phases,[32,33] Si-Ge alloys,[34] etc.[6] with ZT values now reaching the unity. The meteoric rise of thermoelectric sulphides is perhaps best exemplified by the commercialisation of a tetrahedrite-containing thermoelectric module by Alphabet Energy in 2015,[35] only shortly after the first characterisation of the thermoelectric properties of tetrahedrite by Suekuni *et al.* in 2012.[13] Following tetrahedrite's footsteps (but hopefully not its fate as Alphabet Energy ceased all activities in 2018), many newly identified thermoelectric sulphides, and in particular *p*-type ternary and quaternary copper sulphides, have been investigated. A few examples include bornite Cu_5FeS_4,[36–38] germanite derivative $Cu_{22}Fe_8Ge_4S_{32}$,[39,40] stannoidite $Cu_{8.5}Fe_{2.5}Sn_2S_{12}$,[41] mohite Cu_2SnS_3,[42] kesterite Cu_2ZnSnS_4,[43,44] chalcopyrite $CuFeS_2$[45] and the highly promising colusite $Cu_{26}A_2E_6S_{32}$ (*A* = V, Nb, Ta, Cr, Mo, W; *E* = Ge, Sn, As, Sb). It is worth noting that these materials are all derivatives of the sphalerite system, for which the hybridisation of the Cu-3d states and the S-3p orbitals forms the main

contribution to the top of the valence band, see section 3.1. The hybridisation of the Cu-3d states with delocalised chalcogen-p states has been the subject of extensive theoretical studies,[46] and sphalerite-based characteristics have been used for screening potential novel thermoelectric copper sulphides.[47] Binary copper sulphides have also piqued the interest of thermoelectric researchers, long before ternary and quaternary sulphides ever did, by a mere 150 years or so with the work of French researcher Alexandre-Edmond Becquerel.[48] Incidentally, in that same 1866 communication, Becquerel had already foreseen the potential of natural minerals, writing "*The unions of the aforementioned thermoelectric substances are those, as artificially produced, giving the most energetic effects. Perhaps further progress may come with natural minerals;* (…)".† Unfortunately, despite intensive research efforts and the highest ZT values (by far) reported for sulphides, $Cu_{2-x}S$-based materials have yet to produce reliable devices. The main issue, related to the applicability of superionic thermoelectric materials in modules, is still very much controversial.[49,50]

In this report, the crystal structure, crystal chemistry and transport properties of the promising thermoelectric material colusite are reviewed. While the focus is given to thermoelectric performance, we will attempt to give a more general overview of the peculiar behaviour of its transport properties. By doing so, we hope that its complexity might be of interest for other fields. For instance, the related tetrahedrite was considered as a potential solar-absorber for photovoltaic cells following the work of thermoelectric scientists.[51,52] In recent years, sulphides have been attracting considerable attention because of their terrestrial abundance and their role in essential technologies such as Li/Na/K-ion batteries,[53–57] solar cells,[54,58,59] fuel cells,[54,60,61] or biomedical applications.[62–64] Thus, the rich chemistry of colusites could find applications beyond thermoelectricity with a foreseeable impact in the near future.

2. Crystal structure

2.1. Origin

Natural mineral colusite with the general formula $Cu_{24+x}V_2(As,Sb)_{6-x}(Sn,Ge)_xS_{32}$ [65,66] is a somewhat rare mineral that forms in porphyry-type, epithermal and volcanogenic massive sulphide deposits across the globe,[65,67–74] first described in 1933.[75] Unlike its synthetic counterparts, natural colusite always contains V in the *A* site and a majority of As on the *E* site with usually a sizable fraction of Sn, Ge or Sb. Although the generic term "colusite" is favoured for all synthetic derivatives with the general formula $Cu_{26}A_2E_6S_{32}$ (*A* = V, Nb, Ta, Cr, Mo, W; *E* = Ge, Sn, As, Sb), the endmembers of the naturally-occurring isostructural materials are sometimes referred to as nekrasovite (or Sn-rich colusite), germanocolusite (or Ge-rich colusite) and stibiocolusite (or Sb-rich colusite).[66,67,76] In order to avoid confusion, synthetic materials of the colusite family will be referred to as "*A*-*E* colusite" depending on the nature of the cations in the *A*-site and *E*-site positions.

2.2. An ordered sphalerite derivative

Like many ternary and quaternary copper sulphides with promising thermoelectric properties, colusite is strongly related to the non-centrosymmetric sphalerite crystal type,[7] that consists in vertex-linked MS_4 tetrahedra building blocks forming a zinc-blende-like network (space group $F\bar{4}3m$, a_{sph} ≈ 5.1-5.6 Å, 8 atoms per unit cell). In a hypothetical "CuS" sphalerite structure, all CuS_4 tetrahedra are thus corner-sharing and oriented in the same direction in a "Cu_4S_4" cubic cell (Figure 1a). Even though binary copper sulphides do not crystallise in a simple sphalerite framework, but rather form complex derivative structures,[49] many ternary and quaternary copper sulphides exhibit a mixed-cation *M*S sphalerite framework, sometimes with cationic ordering. Many of those are formed naturally such as chalcopyrite $CuFeS_2$, stannite Cu_2FeSnS_4, briartite Cu_2FeGeS_4, famatinite Cu_3SbS_4, roquesite $CuInS_2$, kuramite Cu_3SnS_4, kesterite Cu_2ZnSnS_4, etc. Furthermore, a sphalerite framework can be seen as a host structure that can accommodate a variety of guest species into the array of vacant tetrahedral sites (Figure 1b). Complete occupation of these sites would result in an antifluorite-type structure, M_2S. In many occasions however, the occupation of some of these interstitials in an ordered fashion can give rise to superstructures, as it is the case for colusites and other natural and synthetic minerals such as germanite $Cu_{22}Fe_8Ge_4S_{32}$, stannoidite $Cu_8Fe_3Sn_2S_{12}$ or mawsonite $Cu_6Fe_2SnS_8$. In sphalerite derivatives, ordering of the cations in tetrahedral positions and/or occupation of an interstitial position usually lead to different space groups and larger unit cells. Similarly, the rather complex colusite structure can easily be described as an ordered "$Cu_{24}E_6S_{32}$" sphalerite-network with a unit cell doubled in all three directions, $2a_{sph} \times 2a_{sph} \times 2a_{sph}$ (space group $P\bar{4}3n$, $a = 2a_{sph}$ ≈ 10.5-10.9 Å). In this "$E_6Cu_{24}S_{32}$" sphalerite framework, 6 out of the 32 tetrahedra

contain an atom *E* (*E* = Ge, As, Sb, Sn) while the remaining 24 CuS_4 tetrahedra form the "$Cu_{24}S_{32}$" conductive network, see section 3.1. These tetrahedra are ordered as depicted in Figure 1c. Finally, two "interstitial" atoms per unit cell (*A* = V, Nb, Ta, Cr, Mo, W) occupy the 2*a* position w.r.t. the $P\bar{4}3n$ superstructure, i.e. at the centre and the corners of the $2a_{sph} \times 2a_{sph} \times 2a_{sph}$ supercell, leading to 66 atoms per unit cell (Table 1 and Figure 1c-d). The resulting AS_4 tetrahedra are thus sharing edges with the surrounding CuS_4 tetrahedra in a similar way than VS_4 tetrahedra in sulvanite.[77] Overall, the Cu cations are found in positions 6*d*, 8*e* and 12*f*, *A* cation in position 2*a*, *E* cation in position 6*c* and S in positions 8*e* and 24*i*. As of now, only group 5 and 6 transition metals have been reported as *A* cations and only Ge, Sn, As and Sb have been observed in *E* site in colusites.

Table 1. Atom coordinates for colusites $Cu_{26}A_2E_6S_{32}$. (space group $P\bar{4}3n$, $a \approx 10.5$-10.9 Å)

Atom	Site	Site symmetry	x	y	z
Cu1	*6d*	$\bar{4}$..	¼	0	½
Cu2	*8e*	.3.	$x_{Cu2} \approx$ ¼	x_{Cu2}	x_{Cu2}
Cu3	*12f*	2..	$x_{Cu3} \approx$ ¼	0	0
A	*2a*	23.	0	0	0
E	*6c*	$\bar{4}$..	¼	½	0
S1	*8e*	.3.	$x_{S1} \approx$ ⅛	x_{S1}	x_{S1}
S2	*24i*	1	$x_{S2} \approx$ ⅜	$y_{S2} \approx$ ⅜	$z_{S2} \approx$ ⅛

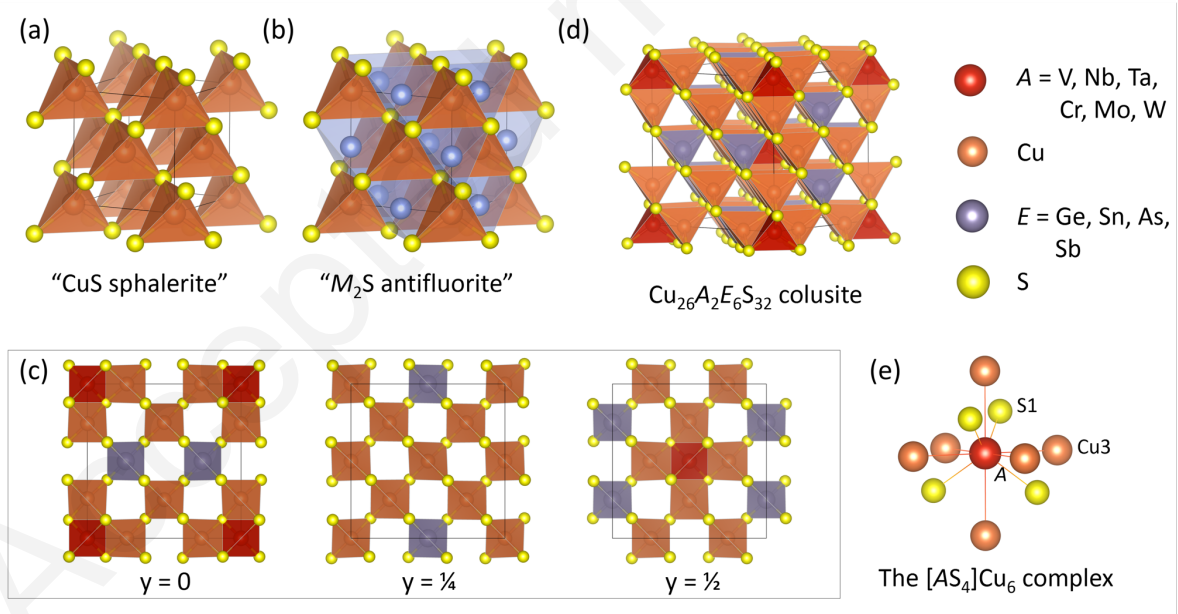

Fig. 1. Structural representation of (a) the hypothetical "CuS" sphalerite, (b) the available tetrahedral interstitial positions in a sphalerite framework, represented by light blue spheres, (c) the layer-by-layer structure of colusite, $Cu_{26}A_2E_6S_{32}$, showing the ES_4 tetrahedra in grey and AS_4 tetrahedra in red, (d) the colusite structure et (e) the $[AS_4]Cu_6$ complex.

2.3. Mixed tetrahedral-octahedral complex

The nature of the species in 2*a* position has been found to be a key factor in controlling the electrical transport properties of colusite despite being relatively excluded from the top of the valence band, see section 3.1. It is thus important to look into the chemical environment surrounding the *A* atom. As depicted in Figure 1e, the cation in the "interstitial" 2*a* position is surrounded by four sulphur atoms (in 8*e* position) forming the AS_4 tetrahedra. On closer inspection, it appears that the 6 neighbouring Cu atoms (in 12*f* position) form an additional octahedral surrounding, resulting in mixed a tetrahedral-octahedral $[AS_4]Cu_6$ complex.[77,78] Pavan Kumar *et al*. reported the synthesis of group 6 colusites, $Cu_{26}A_2Ge_6S_{32}$ (*A* = Cr, Mo, W), for the first time and concluded that the *A* cation was in a +VI oxidation state.[78] They observed that, within these complexes (isolated from one another), the observed interatomic distance between *A* and S was slightly larger than expected from the ionic radii.[79] Conversely, the *A*-Cu distances in the ACu_6 (*A* = Cr, Mo, W) octahedra, determined by combined X-ray powder diffraction (XRPD) and neutron powder diffraction (NPD), were found to be abnormally short for a pure ionic bonding scheme, as supported by bond valence sum calculations. Indeed, the observed values for the *A*-Cu distance in pristine colusites, ranging from 2.708 Å (A = Cr, E = Ge) to 2.771 Å (A = W, E = Ge),[78] are similar to those observed for metal-metal interactions in other inorganic sulphides.[80–84] In the V-Sn colusite, that exhibits some of the best thermoelectric performances among quaternary sulphides, the metal-metal interactions in the cluster remain strong with a V-Cu distance of 2.736 Å. Overall, the abnormally long *A*-S bonds and short *A*-Cu interactions evidence a competition between iono-covalent bonds and metal-metal interactions, resulting in a tetrahedral-octahedral complex whose geometry changes with the nature of the species in the central 2*a* position.[80] This competition arises from the crystal structure of colusite (i.e. insertion of *A* cations into sphalerite framework) but is also strongly influenced by the differences in electronegativity between the *A* cation and the surrounding Cu. Increasing the ionicity of the *A*-S bond thus softens the neighbouring Cu-S bonds.

By studying the Cr-Mo and Cr-W solid solutions of the high-performance Cr-Ge colusite, Pavan Kumar *et al*. gave valuable insights into the chemical bonding of this family of materials and in particular on the role of the cation in 2*a* position, see section 4.4.[80] Successful incorporation of Mo and W in the tetrahedral-octahedral complex was supported by XRPD and the resulting key distances are displayed in Figure 2. While the determined distances support the under-bonding of the 2*a* cation with the surrounding sulphur atoms, the evolution of the distances near the complex upon incorporation of the larger isovalents Mo^{6+} and W^{6+} brings crucial information about the crystal chemistry of colusite. Indeed, the authors concluded that (i) the interatomic distances within the complex vary significantly with the addition of Mo or W, with a much more pronounced effect for

the latter, indicating that a purely ionic model is unsuitable (Figure 2b, c), (ii) the strength of the metal-metal interaction increases as the size of the cation decreases (Figure 2c), (iii) the tetrahedra surrounding the complex are more distorted than the ones found further away and (iv) are more susceptible to vary with the nature of the $[AS_4]Cu_6$ complex (Figure 2d). Overall, the tetrahedra that are connected to the complex, i.e. Cu(8*e*)S_4, can be substantially distorted by modifying the *A* cation while less distortions are observed for tetrahedra that are found further away, i.e. Cu(6*d*)S_4 and Ge(6*c*)S_4, in relation with their localisation on higher symmetry site (Table 1). Because the transport properties of colusite are governed by the Cu-S network, the chemical nature of the *A* cation has an indirect influence over the transport properties through structural distortion of the neighbouring tetrahedra and thus of the conductive network.

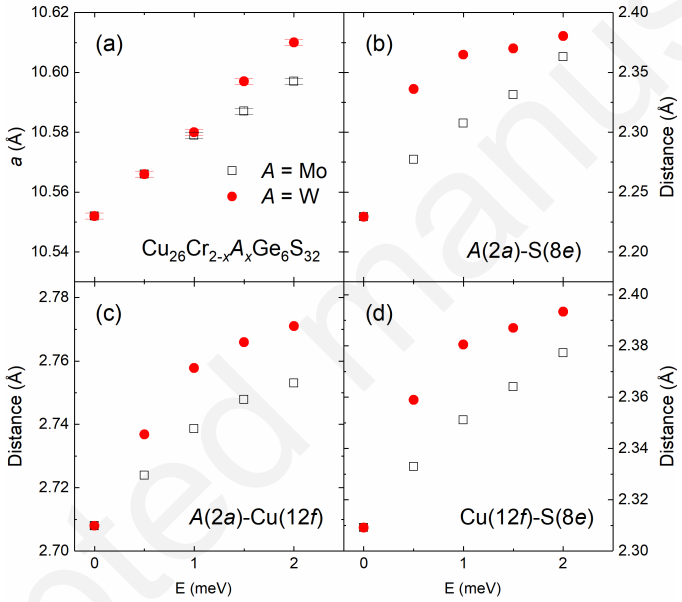

Fig. 2. Evolution of (a) the unit cell parameter; and the (b) *A*(2*a*)-S(8*e*), (c) *A*(2*a*)-Cu(12*f*) and (d) Cu(12*f*)-S(8*e*) distances within the tetrahedral-octahedral complex with x for $Cu_{26}Cr_{2-x}A_xGe_6S_{32}$ (*A* = Mo, W). Adapted from reference [80].

2.4. Synthetic colusite

So far, colusite samples have been synthesised using two different synthesis routes; either by solid state reaction in a sealed silica tube or by mechanical alloying of the precursors followed by in-situ crystallisation during the consolidation step (see section 4, Table 4). The latter is particularly interesting as it offers a potential scale-up solution although samples with better crystallisation are obtained from sealed-tube synthesis. In the vast majority of reports, traces amounts of second phases can be seen, regardless of the synthesis conditions. It is thus difficult to obtain colusite as a

single-phase material. In particular, the synthesis of the V-Sn colusite samples from high-temperature solid-state reaction seems to produce two crystallographically related phases with at least one of them being colusite. The level of caution related to the nature of the second phase, although it appears to be a second colusite phase with slightly different unit cell parameter, stems from the difficulty to correctly identify the peak splitting for the low-angle superstructure peaks. Nonetheless, such peak splitting was observed in the first report of a synthetic colusite, $Cu_{26-x}Zn_xV_2Sn_6S_{32}$, prepared by sealed-tube reaction at high-temperature for thermoelectric properties investigation by Suekuni *et al.*[85] Both $Cu_{26-x}Zn_xV_2Sn_6S_{32}$ and $Cu_{26-x}Zn_xV_2Ge_6S_{32}$ (x = 0, 2, 4) were synthesised using the same high temperature route from high-purity elemental precursors, involving a two-step reacting/sintering at 1273 K and 1073 K after intermediate grinding and compacting. The authors reported the crystallisation of two colusite phases with unit cell parameters, *a*, of 10.759 Å and 10.802 Å. Interestingly, with the substitution of Cu by Zn, the materials become single-phase with a unit cell parameter of 10.788 Å and 10.808 Å for x = 2 and x = 4 respectively. Substitution of Cu by Zn was later confirmed by neutron powder diffraction.[86]

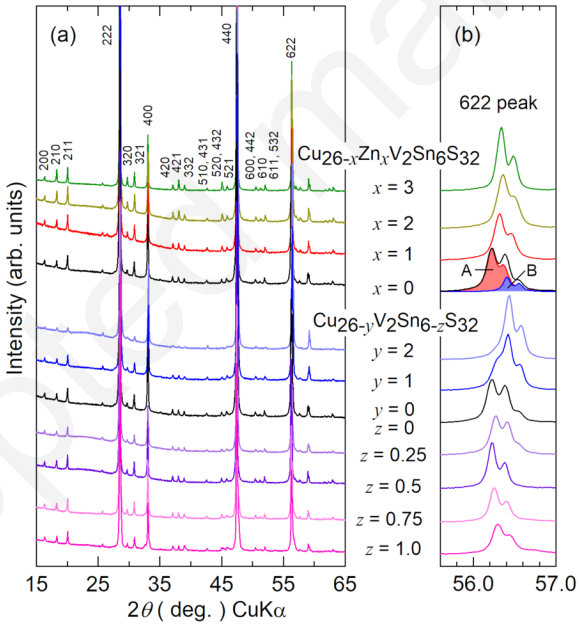

Fig. 3. (a) Powder X-ray diffraction patterns of $Cu_{26-x}Zn_xV_2Sn_6S_{32}$ ($0 \le x \le 3$) and $Cu_{26-y}V_2Sn_{6-z}S_{32}$ ($0 \le y \le 2$; $0 \le z \le 1$). (b) A close-up view of the 622 reflection, showing the deconvolution of the signal from pristine $Cu_{26}V_2Sn_6S_{32}$ into two contributions from the colusite phase A and the Cu-poor phase B. Reproduced from Kim *et al.*, with the permission of AIP Publishing.[87]

The issue related to phase separation is only observed for the V-Sn colusite while the same study reported nearly single-phase pristine V-Ge colusite with only traces of CuS impurities. The reasons behind the phase separation in the pristine V-Sn colusite, while single-phase V-Ge colusite and Zn-

doped V-Sn colusite could be produced, are not discussed and are yet to be fully understood; however, more studies about V-Sn colusite shed some light on the matter. Suekuni *et al*., in a different study,[88] used an additional hot-pressing step in order to obtain samples with higher densities, by doing so they noticed a significant sulphur loss and electron probe microanalysis (EPMA) showed a significant deviation from the stoichiometry with a determined composition of $Cu_{25.97(11)}V_{2.09(6)}Sn_{5.95(7)}S_{30.62(26)}$. This first link between temperature, sulphur loss and unit cell parameter was followed up later on by Bourgès *et al*.,[89] using mechanical alloying as a synthesis route. However, sulphur loss alone cannot account for the phase separation observed for the V-Sn colusite. Kim *et al*.[87] suggested that the second phase (referred to as phase B in Figure 3b) observed in the synthesis of pristine V-Sn colusite, and accounting for 20 % of the product estimated from the deconvolution of the 622 peaks, had a different crystal structure than colusite with a loss of symmetry. This was evidenced by the loss of intensity of the superstructure peaks at low angles when a Cu-poor colusite "$Cu_{24}V_2Sn_6S_{32}$" sample, consisting mainly of phase B, was synthesised (Figure 3a). Moreover, they determined by EPMA than the stoichiometry of the two phases differ mostly by their Cu:(V, Sn) ratio, suggesting that the phase separation was driven by the formation of a Cu-poor phase as opposed to sulphur loss. This is consistent with the disappearance of phase B with increasing z in $Cu_{26}V_2Sn_{6-z}S_{32}$. This was later followed up by Bourgès *et al*., where a direct link was established between the sintering temperature (from mechanically alloyed powders) and the enlarged unit cell parameter, through an increase in cationic disorder.[89] In another study by Bourgès *et al*., the authors attributed the exsolution of the pristine V-Sn colusite to the high purity of the starting materials that deprives synthetic colusite from stabilising impurities like those observed in natural minerals.[86] This observation draws a clear parallel with the cousin mineral tetrahedrite, in which synthetic samples prepared from the nominal stoichiometry consist in two tetrahedrite phases, a Cu-poor $Cu_{\approx 12.3}Sb_4S_{13}$ and a Cu-rich phase $Cu_{\approx 14}Sb_4S_6$.[90,91] As with tetrahedrite, colusite can be synthesised fairly easily when a doping element is added as pristine V-Sn colusite contains a rather high proportion of divalent copper, in term of formal charges: $[Cu^+]_{22}[Cu^{2+}]_4[V^{5+}]_2[Sn^{4+}]_6[S^{2-}]_{32}$. Substituting copper with a divalent transition metal such as Zn^{2+} thus stabilises the structure by reducing the proportion of Cu^{2+}. Nonetheless, later studies demonstrated the feasibility of producing a pure pristine V-Sn colusite by increasing the hot-press sintering time from a few minutes to 1h for powders prepared by sealed-tube synthesis[92] or by using mechanical alloying and spark plasma sintering (SPS) of elemental[89] or binary precursors.[93] In the former route, the annealing effect promotes the coalescence of the two related phases into one while the fine reactive mechanically alloyed powders yield single-phase materials after SPS in the latter. Therefore, it appears that the exsolution of pristine V-Sn colusite, while indirectly linked to sulphur loss because of the required

synthesis conditions, is more likely to be imputed to inhomogeneity in bulk powders that can be overcome by longer annealing or mechanical alloying. The latter was found to be a successful and scalable way to produce hundreds of grams of performing, phase-pure, V-Sn colusite from industrial-grade binary sulphides and elemental vanadium precursors.[93] It appears that other compositions, in particular the *A*-Ge colusites, are easier to produce as single phases, though it should be noted that V-Sn and V-Ge colusites were the first one to be synthesised and the subsequent studies thus benefitted from earlier findings.

Following the pioneering work of Suekuni *et al*.,[85,88,94] researchers first tried to shy away from using vanadium as there might be practical concerns related to the toxicity of vanadium oxides.[95,96] This led Kikuchi *et al*. to synthesise the first Nb-Sn and Ta-Sn colusites by solid-state reaction, although the latter contained non-negligible amounts of binary copper sulphide impurities.[92] The series was extended by Bouyrie *et al*. to the Ge-colusite with Nb-Ge and Ta-Ge, where impurities were also found.[97] The presence of impurities in Ta-*E* colusite was imputed to the higher melting point and lower reactivity of tantalum.[97] Note that in the V-Sn colusite prepared from binary precursors, the elemental vanadium was the last element to react, with the mixture initially forming a ternary Cu-Sn-S phase.[93,98] The effect of annealing and cation off-stoichiometry on the Nb-Ge colusite confirmed the observations made on V-Sn colusite with the enlargement of the unit cell with annealing temperature and the link with sulphur loss and cation off-stoichiometry.[99] Moreover, in the same investigation, Suekuni *et al*. demonstrated that modifying the Sn:Cu ratio in the Nb-Sn colusite led to a loss of symmetry with the complete disappearance of the characteristic superstructure reflections of colusite, pointing toward an fcc symmetry for x = 1.2 in $Cu_{26-x}Nb_2Sn_{6+x}S_{32}$.[99] This is reminiscent of the second phase observed for some V-Sn colusites and suggests that changing the balance between *E*-site cation and Cu in colusite will result in single-phase material with loss of symmetry. Conversely, temperature-induced sulphur volatilisation only causes a cationic rearrangement, with retention of the symmetry elements of the $P\bar{4}3n$ space group. The possibility to accommodate extra cations in colusite has been exploited by researcher in order to reproduce the effect of cationic disorder, without the need for high-temperature processes.[100–102]

Finally, the latest addition to the colusite family came with the first synthesis of group 6 colusite, $Cu_{26}A_2Ge_6S_{32}$ (*A* = Cr, Mo, W), by Pavan Kumar *et al*..[78] The samples were successfully synthesised by mechanical alloying and SPS and were crucial to understand the structure-property relationships and in particular the role of the *A*-site cations in the transport properties of colusites.[80,101] So far, there has not been any reported successful synthesis of a colusite involving As or Sb on the *E* site despite their occurrence in natural minerals.

3. Crystal chemistry

3.1. Electronic structure

The first synthetic colusites, $Cu_{26}V_2E_6S_{32}$ (*E* = Sn, Ge), were described as Pauli paramagnets based on the weak temperature dependence of their magnetic susceptibility, consistent with a formal valence of +V for vanadium.[85] The authors proposed an electronic structure based on those of related phases Cu_3VS_4, Cu_2ZnSnS_4 and Cu_2ZnGeS_4, and correctly predicted that the top of valence band (VB) must be composed of hybridised Cu-3d and S-3p orbitals and the bottom of the conduction band (CB) of V-3d/S-3p and *E*-*n*s/S-3p (*E* = Ge, Sn; *n* = 4, 5) in presence of a band gap. Subsequently, the electronic band structures have been reported for $Cu_{26}V_2Sn_6S_{32}$ and $Cu_{26}A_2Ge_6S_{32}$ (*A* = V, Cr, Mo, W) with band gaps between 0.5 eV and 1 eV depending on the nature of the *A* and *E* cations.[78,80,88,89] These studies confirmed the formal charges in colusites by combining Mössbauer spectroscopy, structural analyses and electrical properties measurements. In group 5 colusites, $Cu_{26}A_2E_6S_{32}$ (*A* = V, Nb, Ta; *E* = Ge, Sn), as mentioned in the previous section, the formal balance can be written as $[Cu^+]_{22}[Cu^{2+}]_4[A^{5+}]_2[E^{4+}]_6[S^{2-}]_{32}$. The Sn atoms have been confirmed to be in a +IV oxidation state by ^{119}Sn Mössbauer spectroscopy.[86,103] In group 6 colusites, $Cu_{26}A_2Ge_6S_{32}$ (*A* = Cr, Mo, W), the *A*-site cations was demonstrated to be in a +VI oxidation state,[78] reducing the amount of divalent copper by half compared to group 5 colusites: $[Cu^+]_{24}[Cu^{2+}]_2[A^{6+}]_2[Ge^{4+}]_6[S^{2-}]_{32}$. Overall, in order to be able to stabilise the colusite structure by incorporating a cation at the centre of the mixed tetrahedra-octahedral complex, it appears that a d^0 electronic configuration is required for *A*. It is perhaps not surprising considering the complex chemical surroundings and the presence of strong metal-metal interactions.

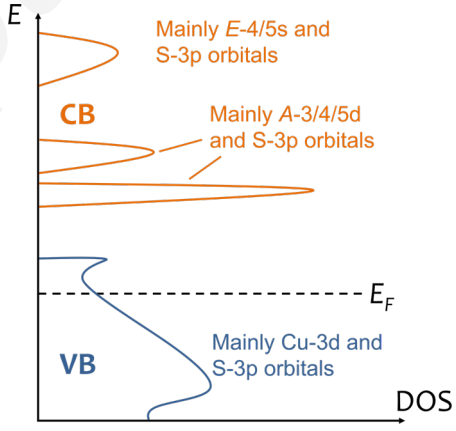

Fig. 4. Schematic band structure for colusites, $Cu_{26}A_2E_6S_{32}$ (*A* = V, Nb, Ta, Cr, Mo, W; *E* = Ge, Sn), based on reported electronic density of states and predictions. The peculiar shape of the top of the valence is a graphical representation based on the reported band structures.

From the reported electronic density of states for $Cu_{26}V_2Sn_6S_{32}$ and $Cu_{26}A_2Ge_6S_{32}$ (*A* = V, Cr, Mo, W), with all compositions exhibiting very similar features,[78,85,88,89] it is possible to draw a generalised electronic band structure for colusites (Figure 4). As mentioned previously, the top of the valence band is mainly composed of hybridised Cu-3d and S-3p orbitals, where the Fermi level lies within the band, giving rise to *p*-type metallic conduction for un-doped colusite. Note that the multivalley character of the top of the VB and the accompanying large effective masses are desirable characteristics for thermoelectric application.[104] Interestingly, the S atoms contributing the most to the top of the VB are those found in 24*i* position, i.e. away from the tetrahedral-octahedral complex, consistent with the concept of conductive network within the sphalerite framework. Above the band gap, the first onset of conduction bands is mainly composed of the *A*-cation *d* orbitals and S-3p orbitals with the formers split by crystal-field effect into *e* and t_2 bands. Overall, the electronic structure of colusite is consistent with ionic bonds between the *A* cation and the surrounding S atoms, that in turn, seem to soften the Cu(12*f*)-S(8*e*) bonds.[89] , Ochi *et al*. studied in-depth the links between the electronic band structure of materials with Cu*Ch*$_4$ (*Ch* = S, Se) tetrahedra and good thermoelectric performances, focusing on the role of the Cu-3d states in low-dimensional complex.[105]

The concept of conductive network, which arises from the hybridised Cu-3d and S-3p orbitals in the sphalerite framework and the Cu(I)-Cu(II) mixed valence, is important as it establishes a link between colusites and other performing materials derivative of the sphalerite structure. Interestingly, a parallel can be drawn between the Cu(I)-Cu(II) mixed valence in thermoelectric copper sulphides, such as colusites, and the concept of Cu(II)-Cu(III) mixed valence in superconductivity.[106] These key features were already spotted in the parent mohite, Cu_2SnS_3, where first-principle calculations demonstrated the existence of a similar 3D Cu-S (and S-S) conductive network.[107] The authors correctly predicted excellent thermoelectric properties in Cu_2SnS_3, resulting from heavy, yet conductive, hybridised Cu-3d/S-3p bands.[108] A later study by Shen *et al*. confirmed that Zn-doped Cu_2SnS_3 was in fact a very good eco-friendly thermoelectric material.[42] Moreover, Xi *et al*. suggested that doping on Sn sites was likely to be the most efficient carrier-tuning strategy because of the very limited involvement of Sn at the top of the VB. This was later found to be a relatable observation in V-Sn colusite, where introducing Cu/Sn cationic disorder was beneficial for thermal transport properties while retaining excellent electrical performances.[89,103] Recent research also demonstrated that the conductive network of colusite could be functionalised indirectly by the remote action of the *A* cation in "interstitial" position.[78,80,101] Finally, it appears that strategies involving stoichiometric variations of the *E*-site cation were overall better at tuning the thermoelectric properties than doping on the Cu sites.[87,97]

3.2. Vibrational structure

Some crystallographic characteristics, found in popular TE materials, are known to lead to complicated vibrational structures that can be powerful tools in order to lower the thermal conductivity, one of the main concerns of thermoelectric researchers. Performing TE materials with ultralow thermal conductivity often depend on characteristics such as large cages for rattling atoms, e.g. skutterudites or argyrodites,[30,109] out-of-plane Cu vibration, e.g. tetrahedrites[110] or $Cu_4Sn_7S_{16}$,[98,111] low-dimensional structures, e.g. Bi_2Te_3,[112] etc. Unfortunately, the crystal structure of colusites does not possess such special feature, aside from a relatively exotic mixed tetrahedral-octahedral [AS_4]Cu_6 complex that does not appear to have a great impact on the thermal transport properties. Nonetheless, the thermal conductivity of pristine colusites remains reasonably low despite high electrical conductivity, see section 4.1, owing to a large unit cell containing a large number of atoms of various sizes. The phonon dispersions and corresponding vibrational densities of states (VDOS) for some colusites were computed (Figure 5) using density functional theory (DFT).[78,89] For $Cu_{26}V_2Sn_6S_{32}$, two observed features are of particular interest for thermoelectric application, i.e. with the potential of leading to low thermal conductivity. First, in the phonon dispersion, the compressed acoustic branches are known to lead to low heat carrier velocity and thus to low thermal conductivity.[113,114] This was also true for the Cr-Ge and Mo-Ge colusites, not shown here.[78] Additionally, low frequency optic modes are observed for all investigated colusites and are known to interact with acoustic vibration modes for additional scattering channels. Such optic modes are found at frequencies around 40 cm^{-3} and 60 cm^{-3} with a large contribution from the Cu in 12*f* position. Note that the contribution was mistakenly attributed to Cu(8*e*) in the text of the original publication.[89] This is particularly visible from the atom-projected VDOS of $Cu_{26}V_2Sn_6S_{32}$, and perhaps less evident and shifted to higher frequencies for the Cr-Ge and Mo-Ge colusites, where contributions from other Cu positions are also significant in the low-frequency region. In all cases however, the *A* cation at the core of the tetrahedral-octahedral complex contributes only mildly to the low-frequency optic modes. Because of the light mass of Cu and the additional metal-metal interaction with the cation in 2*a* position, we can extrapolate that colusites possess rather soft Cu(12*f*)-S bonds, consistent with a major impact on the thermal transport properties. This is corroborated by the computed total energy response to bond compression being softer for Cu(12*f*) than Cu(8*e*) or Cu(6*d*).[89] Note that the weak copper bonding, comparable to a supressed Cu ion conduction, has been shown to greatly impact the thermal conductivity through localised low-energy vibrational modes.[110]

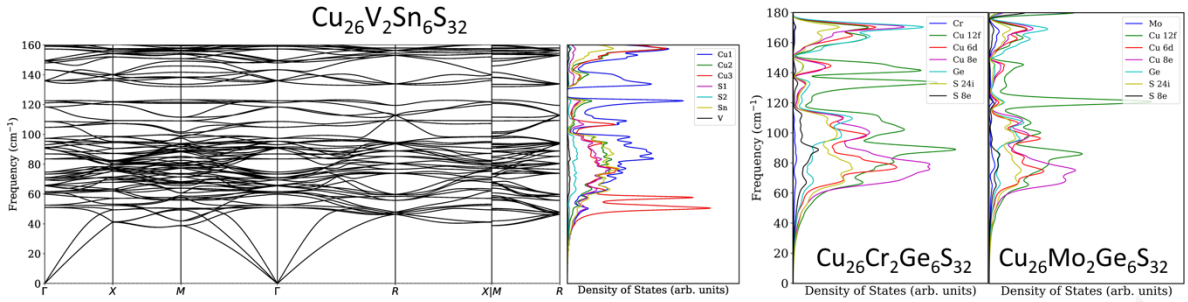

Fig. 5. Phonon dispersions for $Cu_{26}V_2Sn_6S_{32}$ and atom-projected vibrational density of states for $Cu_{26}V_2Sn_6S_{32}$, $Cu_{26}Cr_2Ge_6S_{32}$ and $Cu_{26}Mo_2Ge_6S_{32}$. Adapted from references [78] and [89].

In order to obtain a fundamental understanding of the effect of structural disorder on the thermal transport properties of the V-Sn colusite, Candolfi *et al*. measured the generalised phonon density of states, $G(\omega)$, using inelastic neutron scattering, for two samples, the (mostly) ordered and the (mostly) disordered V-Sn colusites (Figure 6), noted samples L and H respectively.[103] In both cases, the obtained $G(\omega)$ are consistent with the calculated phonon dispersion and projected vibrational density of states (Figure 5), with the presence of three blocks of vibrational modes between 5 and 12 meV, 12 and 22 meV, and beyond 30 meV.[89,103] The temperature dependence of the generalised phonon density of states, $G(\omega)$, is consistent with a quasiharmonic model of phonon softening evidenced by a relatively insignificant shift in energy upon warming. Thus, both the phonon frequencies and the interatomic force constants solely depend on the thermal expansion of the unit cell volume. This classical behaviour contrasts with the one observed for tetrahedrites where the high degree of anharmonicity causes the low-energy optical modes to shift to higher energies upon warming. Nonetheless, the thermal conductivity of V-Sn colusites remains low (see section 4) and the high calculated average Grüneisen parameters, $\overline{\gamma_G}$, of 1.96 and 1.45 for the L and H samples respectively, are indicative of bonding anharmonicity. The impact of structural disorder on the thermal transport properties is further detailed in section 4.2. Note that the Grüneisen parameters for the Mo-Ge colusite, determined from theoretical calculations, are also high with $\overline{\gamma_G}$ values of 2.25, 2.27 and 2.34 for the three acoustic modes velocities.[78]

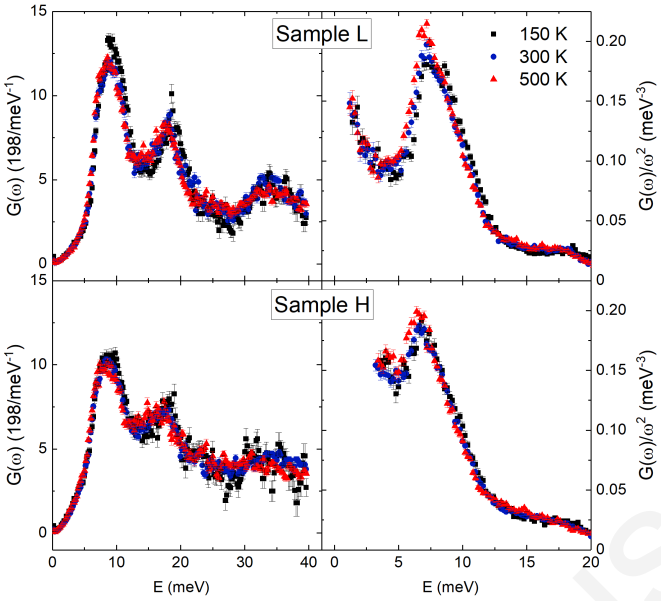

Fig. 6. Generalised vibrational density of states, $G(\omega)$, at 150 K, 300 K and 500 K for (a) sample L and (b) sample H, and corresponding Debye plots , $G(\omega)/\omega^2$, for (c) sample L and (d) sample H. Adapted from reference [103].

Finally, calculated and measured values for the sound velocities have been reported for some colusites (Table 2). The first values were reported by Bouyrie *et al*. for $Cu_{26}Nb_2Sn_6S_{32}$ and $Cu_{26}Nb_2Sn_{5.5}S_{32}$,[97] prepared by conventional high-temperature sealed-tube reaction, followed by works on the V-Sn colusite with an emphasis on the effect of sintering temperature on the structural disorder and ultimately on the thermal transport properties.[89,103] It is worth noting that the computed and experimental sound velocities for Nb-Sn and V-Sn colusites, determined by different research groups, point toward rather high values. These are similar to those observed for some metals such as copper or zinc, suggesting that the chemical bonding in colusites remains rather stiff. This is an important point as it helps to understand why defect chemistry in colusite is, not only rich, but favourable for optimising the thermal transport properties and TE performances.

Table 2. Reported values for the longitudinal, v_L, transverse, v_T, and average, v_{avg}, sound velocities, and longitudinal, ϑ_L, transverse, ϑ_T, and average, ϑ_D, Debye temperatures for colusite samples.

Sample	v_L (m s^{-1})	v_T (m s^{-1})	v_{avg} (m s^{-1})	ϑ_L (K)	ϑ_T (K)	ϑ_D (K)	Reference
$Cu_{26}Nb_2Sn_6S_{32}$	4438	2219	2959[a]	492	246	-	[97]
$Cu_{26}Nb_2Sn_{5.5}S_{32}$	4469	2260	2996[a]	495	250	-	[97]
$Cu_{26}V_2Sn_6S_{32}$ computed	4485	2350/2613	3150	-	-	367	[89]
$Cu_{26}V_2Sn_6S_{32}$ computed	4867	2436	2592	-	-	293	[103]
$Cu_{26}V_2Sn_6S_{32}$ sample L	4260	2120	2833[a]	-	-	280	[89,103]
$Cu_{26}V_2Sn_6S_{32}$ sample H	3620	1830	2427[a]	-	-	235	[103]
$Cu_{23}Zn_3V_2Sn_6S_{32}$	-	-	-	-	-	284	[94]

[a] calculated from reported values using $(2 \times v_T + v_L)/3$

3.3. Defect chemistry

The presence of defects and the tendency to form impurities was noted in the first report of thermoelectric properties of a colusite, when Suekuni *et al*. observed the formation of two structurally different, but related, quaternary phases.[85] The authors also noticed a rise in the magnetic susceptibility at low temperature attributed to a contribution from paramagnetic impurities and/or induced magnetic moment on Cu vacancies. Details about impurities and phase separation are given in section 2.4. These early observations suggested that a rich defect chemistry could be anticipated in colusites. Owing to relatively large number of voids in the structure, such as the interstitial site 6*b* (0, 0, ½) and 24*i* (≈0.25, ≈0.25, ≈0), where the dimension of the empty tetrahedral sites coincides with that of a CuS_4 tetrahedra,[92,99] researchers observed the impact of additional cations. Investigations of the structural and thermoelectric properties were carried out either by directly supplying an over-stoichiometry of cations,[100,101] or by causing sulphur volatilisation.[89,93,99,103,115] Note that, in natural colusite minerals, a higher cation to anion ratio has been observed, up to a 36:32 ratio.[65] Additionally, structural disorder can be encouraged by non-stoichiometry, in particular by varying the Cu:*E* ratio in $Cu_{26}A_2E_6S_{32}$.[97,99]

The first in-depth study of the defect chemistry in a colusite was carried out by Bourgès *et al*. on $Cu_{26}V_2Sn_6S_{32}$,[89] following conflicting reports of TE properties, in particular regarding the thermal transport properties of this phase.[85–88,92] The authors compared the crystal structures and the cationic arrangements of samples prepared from mechanical alloying of elemental precursors and consolidated in different conditions, i.e. spark plasma sintering (SPS) at 873 K and hot pressing (HP) at 1023 K, for sample L and H respectively. The study was followed up by Candolfi *et al*. with the addition of ^{119}Sn Mössbauer spectroscopy and inelastic neutron scattering (INS) analysis[103] and subsequently scaled-up.[93] Similarly, Suekuni *et al*. used non-stoichiometry and sintering temperature variation to generate disorder in the parent Nb-Sn colusite.[99] Overall, the V-Sn and Nb-Sn colusites both exhibit similar defect chemistry: (i) with increasing annealing temperature, the unit cell parameter is shifted to higher values and the amount of atomic-scale structural defects increases while retaining the $P\bar{4}3n$ crystal structure.[89,99,103] (ii) Decreasing the Cu/Sn ratio first leads to a phase exsolution into Sn-rich and Sn-poor phases and (iii) further lowering of the Cu/Sn ratio can lead to a disordered cationic arrangement and a change of symmetry from $P\bar{4}3n$ to $F\bar{4}3m$.[87,99]

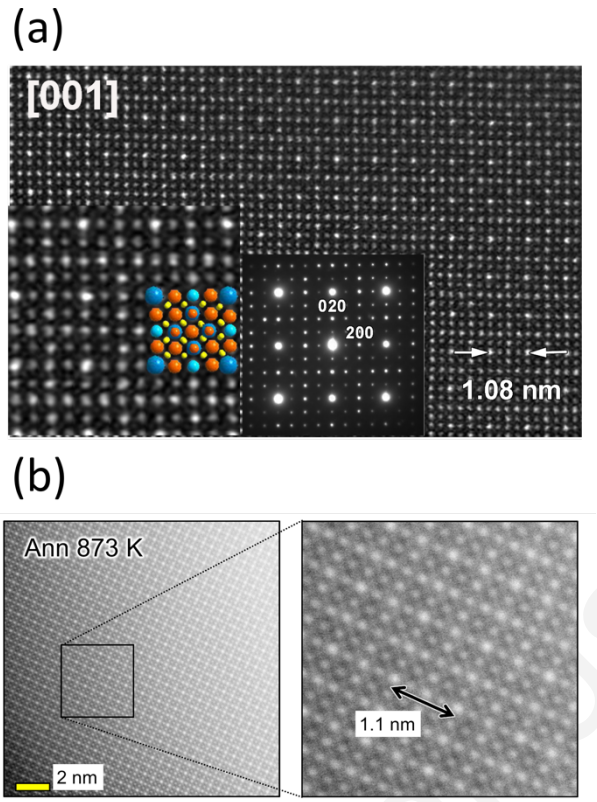

Fig. 7. (a) HAADF-STEM images for $Cu_{26}V_2Sn_6S_{32}$ (sample L) and (b) ADF-STEM images for $Cu_{26.3}Nb_2Sn_{5.7}S_{32}$ both sintered at 873 K. Both show a well-ordered structure with intensity variations consistent with the structural model of colusite. Adapted from references [89] and [99].

In pristine V-Sn and Nb-Sn colusites, i.e. stoichiometric and sintered at low temperature samples, high-resolution transmission electron microscopy (HRTEM) studies, including high angle annular dark field scanning TEM (HAADF-STEM), revealed a highly ordered structure with no apparent defects (Figure 7a, b).[89,99] These initial assessments of the high level of cationic ordering have been somewhat reviewed in a subsequent studies by Candolfi *et al.*, where ^{119}Sn Mössbauer spectroscopy clearly identified a second contribution to the main signal cause by the presence of Sn on a lower symmetry site.[103] By carrying out least-square fitting of sharpened Mössbauer data, and considering the symmetry of the available sites, the authors concluded that, in the sample sintered at low temperature, i.e. the "ordered" sample L, at least 18 % of Sn atoms are found on sites with lower symmetry than the expected 6*c*. Note that it is not possible to conclude that the remaining 82 % are all located on 6*c* as Sn_{Cu} defects on 6*d* are indistinguishable because of the same local symmetry $\bar{4}$ of sites 6*c* and 6*d*. However, from crystallographic data, we can consider that most Sn cations do occupy the 6*c* site. It is fair to assume that this is also the case for the Nb-Sn colusite, despite an evidently well-ordered structure from ADF-STEM images (Figure 7b).[99] We could speculate that the

need for a slightly higher Cu/Sn ratio for optimised TE performances, $Cu_{26.3}Nb_2Sn_{5.7}S_{32}$, might originate from a reduced percentage of Sn on Cu sites. The tendency of forming Sn_{Cu} antisite defects in V-Sn colusite is consistent with total energy calculations (Table 3). Because the favoured 6*d* and 8*e* sites are surrounding the Sn position, this leads to a tendency to form 1D-line defects. These line defects are clearly observable in the samples sintered at higher temperature (Figure 8a) where the ratio of Sn_{Cu} defects increases significantly, as shown from Mössbauer spectroscopy with at least 65 % of Sn atoms located on a lower symmetry site than expected.[103] Similarly, the Nb-Sn colusite sintered at higher temperature also exhibits some level of Cu-Sn antisite formation (Figure 8b).[99]

Table 3. Reported formation energies for antisite defects in $Cu_{26}V_2Sn_6S_{32}$. From Bourgès *et al*.[89]

Defect	**Sn_V**	**Sn_{Cu}**	**Sn_{Cu}**	**Sn_{Cu}**	**V_{Cu}**	**V_{Cu}**	**V_{Cu}**
site	2a	12f	6d	8e	12f	6d	8e
Δ*E* (meV)	33	42	19	25	21	40	31

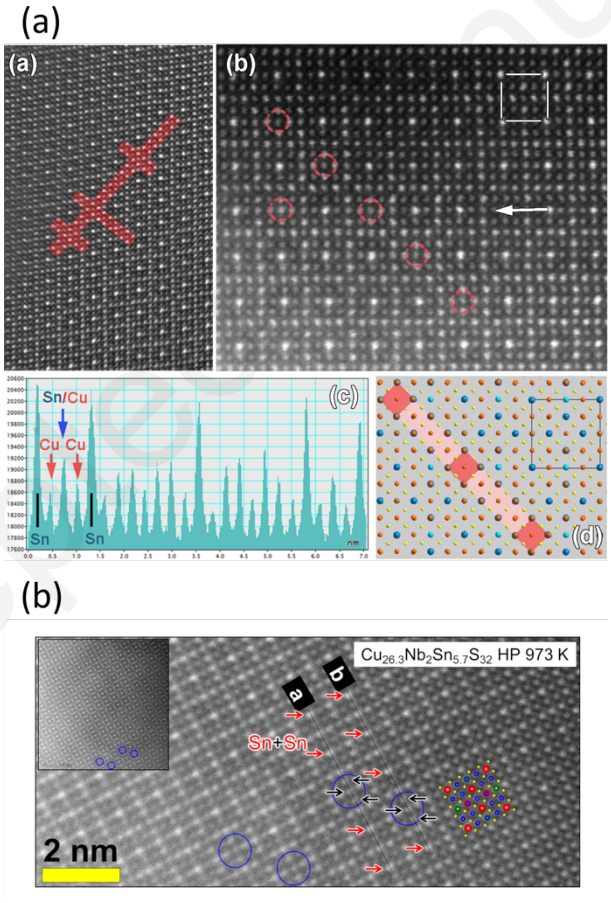

Fig. 8. Evidences for Cu-Sn antisite defects in (a) $Cu_{26}V_2Sn_6S_{32}$ (sample H) and (b) $Cu_{26.3}Nb_2Sn_{5.7}S_{32}$ sintered at higher temperatures (1023 K and 973 K respectively). The images include (HA)ADF-STEM images along the [001] and [100] direction respectively. The corresponding intensity profiles clearly

show variations in the relative intensities, indicating exchange between Cu and Sn atoms. Adapted from references [89] and [99].

The additional heat treatment inflicted to the sample H of V-Sn colusite led to the appearance of fully disordered regions (Figure 9a) similar to those observed in the fully disordered $Cu_{24.8}Nb_2Sn_{7.2}S_{32}$ with fcc symmetry (Figure 9b). However, in the former, these regions are found within the same crystallite than fully ordered areas, coherently intergrown with equivalent structural framework and unit cell. In natural samples, similar order/disorder domains were also observed, with the assumption made by Spry *et al*. that the disordered phase is the high-temperature stable form.[65] The cationic arrangement can therefore be altered locally in a way that generates 1D line defects and, in some regions, 3D disorder where all cations statistically occupy a fraction of the cation sites of the $P\bar{4}3n$ crystal structure. If the balance between the cations is sufficiently modified, i.e. when the Sn/Cu ratio is largely increased, the cationic disorder is accompanied by a loss of symmetry. The presence of cations in interstitial position, although never observed directly, seems highly likely. Indeed, samples that underwent extended heat treatment, and thus suffered sulphur-deficiency and unit cell expansion, are usually accompanied by an increase in the measured density, sometimes above the crystallographic value. This along typically cation-rich EDS analyses point toward cation intercalation instead of sulphur vacancies.[93,99]

Finally, using industrial-grade binary sulphides and metal vanadium for the scaled-up production of V-Sn colusite led to the formation of additional defects arising from the synthesis mechanism.[93] For high sintering temperature (T_{SPS} = 1083 K), the defects observed are similar to the aforementioned ones, including sulphur loss and cationic disorder at the local scale and over large domains within a crystallite (Figure 10e). Conversely, for samples sintered at the minimum required temperature of 873 K to reach sufficiently high density, the binary sulphide precursors evidently reacted first, leaving metal vanadium to form the colusite structure through diffusion into a Cu-Sn-S matrix. This is consistent with a previous *in-situ* neutron diffraction investigation of $Cu_4Sn_7S_{16}$ that observed the rapid reaction of the vanadium sample holder with the Cu-Sn-S phase above 960 K.[98] As a result of the rapid sintering and the low temperature, nano- and micro-scale defects were observed. At the micro-scale, incomplete diffusion of vanadium led to the presence of residual vanadium-rich core shell structures (Figure 10a) while the inhomogeneous cationic distribution resulted in nano-scale Cu-rich or V-rich regions (Figure 10b) and local intergrowth of colusite and sulvanite crystallites (Figure 10c, d). Expectedly, all the aforementioned structural and microstructural defects have a significant impact on the thermoelectric properties of colusites and can be controlled through the synthesis and consolidation processes.

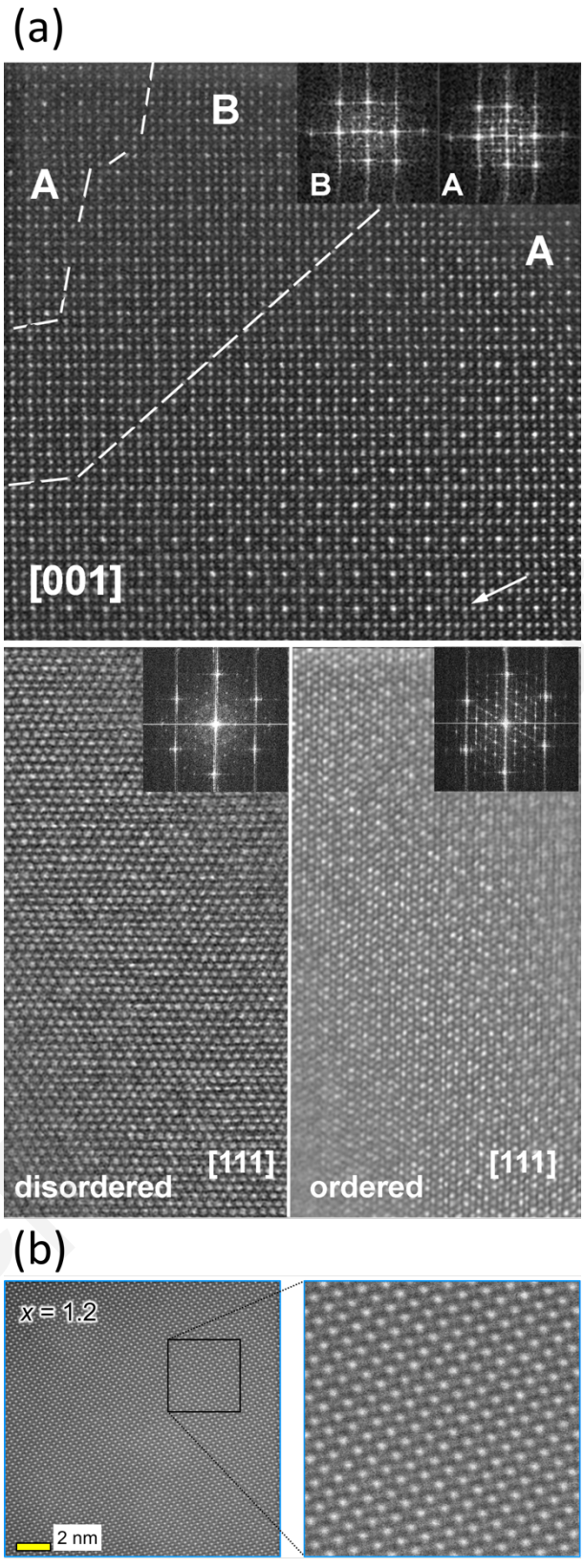

Fig. 9. (HA)ADF-STEM images for (a) $Cu_{26}V_2Sn_6S_{32}$ (sample H, sintered at 1023 K) and (b) $Cu_{24.8}Nb_2Sn_{7.2}S_{32}$. In the V-Sn colusite, the temperature induced 3D disordered regions B, coherently intergrown with ordered regions A. Adapted from references [89] and [99].

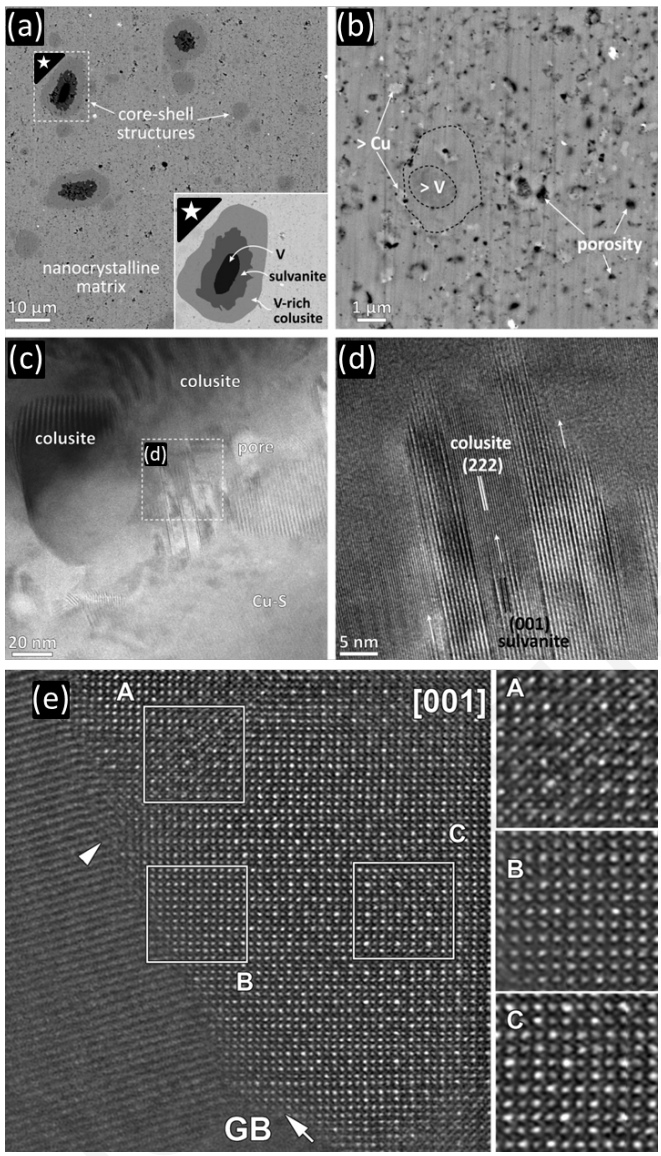

Fig. 10. Microstructural analysis of V-Sn colusite prepared from binary precursors. (a, b) Backscattered SEM and (c, d) TEM images of V-Sn colusite sintered at low temperature, i.e. 873 K. (e) HAADF-STEM image around a grain boundary of a sample sintered at 1083 K, showing well-ordered region C and disordered regions A and B. Adapted from reference [93].

4. Transport properties

The thermoelectric performances of colusite materials depend on a number of factors that makes it rather difficult to have a clear view of the impact of .each individual parameter such as composition, process, doping or defect chemistry. For instance, the transport properties of pristine materials can be severely altered by the synthesis conditions such as sulphur volatilisation during sintering.[89] Therefore, comparing the thermoelectric properties of pristine *A*-*E* colusites in order to deduct the influence of the *A* and *E* cations can be seriously overshadowed by thermal effects over stoichiometry and cation order/disorder. The same is true for doping investigations, where hole doping might have a different impact on the transport properties of a stoichiometric sample compared with a sulphur-deficient material.[88] As a result, defect chemistry has been studied in-depth and was particularly successful in achieving high ZT values for the *A*-Sn (*A* = V, Nb) colusites (detailed in section 4.2).[89,99] Following the excellent performance of these materials, research was extended to other Sn- and Ge-colusites.

In a first part, the performance of pristine colusites will be discussed, including reported transport properties of stoichiometric samples and, as best we can, excluding the effect of impurities, off-stoichiometry or process. In a second part, the impact of process-induced sulphur volatilisation and structural disorder will be discussed, including samples that were regarded as pristine at the time. Finally, the effect and conclusions drawn from different doping strategies and from the transport properties of solid solutions will be addressed.

Table 4. Thermoelectric properties of notable colusites. The top block corresponds to annealed cold-pressed samples; the middle block corresponds to HP or SPS samples sintered at high temperature and exhibiting processed-induced transport properties; the bottom block corresponds to HP or SPS samples sintered at low temperature.

Composition	Synthesis/ consolidation	$T_{sinter.}$ (K)	T (K)	ρ (mΩ cm)	S (μV K^{-1})	S^2/ρ (mW $m^{-1}K^{-2}$)	κ (mW $m^{-1}K^{-1}$)	ZT	Ref.
$Cu_{26}V_2Sn_6S_{32}$	STS / CP + Ann.	1073	300	0.4	27	0.18	2.7	0.02	[85]
$Cu_{26}V_2Ge_6S_{32}$	STS / CP + Ann.	1073	300	0.4	27	0.18	3.2	0.02	[85]
$Cu_{24}Zn_2V_2Sn_6S_{32}$	STS / CP + Ann.	1073	300	2.1	72	0.25	1.2	0.06	[85]
$Cu_{24}Zn_2V_2Ge_6S_{32}$	STS / CP + Ann.	1073	300	2.1	72	0.25	1.4	0.05	[85]
$Cu_{22}Zn_4V_2Sn_6S_{32}$	STS / CP + Ann.	1073	300	98	200	0.4	1.3	0.09	[85]
$Cu_{22}Zn_4V_2Ge_6S_{32}$	STS / CP + Ann.	1073	300	357	260	0.2	1.3	0.04	[85]
$Cu_{26}V_2Sn_6S_{32}$	STS / HP	1073	663	10.3	215	0.48	0.55	0.56	[88]
$Cu_{26}Nb_2Sn_6S_{32}$	STS / HP	1023	660	7.3	≈200	0.56	0.57	0.66	[92]
$Cu_{26}Ta_2Sn_6S_{32}$	STS / HP	1023	660	5.7	≈200	0.69	0.59	0.78	[92]
$Cu_{26}V_2Sn_{5.5}S_{32}$	STS / HP	1073	660	7.1	205	0.59	0.6	0.62	[87]
$Cu_{26}Nb_2Sn_{5.5}S_{32}$	STS / HP	1023	670	5.1	194	0.75	0.63	0.76	[97]
$Cu_{26}Ta_2Sn_{5.5}S_{32}$	STS / HP	1023	670	5.3	205	0.79	0.56	0.96	[97]
$Cu_{26.3}Nb_2Sn_{5.7}S_{32}$	STS / HP	973	670	7.49	213	0.60	0.62	0.66	[99]
$Cu_{26.5}Nb_2Sn_{5.5}S_{32}$	STS / HP	973	663	4.7	198	0.83	0.67	0.83	[116]
$Cu_{26}V_2Ge_6S_{32}$	STS / HP	1073	663	7.1	215	0.61	0.55	0.73	[88]
$Cu_{26}Nb_2Ge_6S_{32}$	STS / HP	1023	670	7.8	225	0.65	0.48	0.93	[97]
$Cu_{26}Ta_2Ge_6S_{32}$	STS / HP	1023	670	10.5	227	0.49	0.51	0.66	[97]
$Cu_{24}Co_2V_2Ge_6S_{32}$	STS / SPS	1073	690	21	265	0.33	0.55	0.42	[102]
$Cu_{24}Ni_2V_2Ge_6S_{32}$	STS / SPS	1073	690	3.5	145	0.6	0.8	0.5	[102]
$Cu_{26}V_2Sn_6S_{32}$ (up-scaled)	MA (indus. grade) / SPS	1083	673	1.93	142	1.04	1	0.7	[93]
$Cu_{26}V_2Sn_6S_{32}$ (Sample H)	MA / HP	1023	675	4.27	175	0.72	0.56	0.93	[89]
$Cu_{26}V_2Sn_6S_{32}$ (Sample L)	MA / SPS	873	675	1.18	90	0.69	1.73	0.27	[89]
$Cu_{26}V_2Sn_6S_{32}$	MA / SPS	873	700	1.25	94	0.64	1.67	0.30	[86]
$Cu_{26}Nb_2Sn_6S_{32}$	MA / SPS	873	675	0.83	75	0.68	2.42	0.19	*
$Cu_{26}Ta_2Sn_6S_{32}$	MA / SPS	873	675	0.86	75	0.63	2.11	0.20	*
$Cu_{26.3}Nb_2Sn_{5.7}S_{32}$	STS / HP	873	670	2.08	115	0.63	1.37	0.31	[99]
$Cu_{25}ZnV_2Sn_6S_{32}$	MA / SPS	873	700	1.35	112	0.92	1.62	0.40	[86]
$Cu_{24}Zn_2V_2Sn_6S_{32}$	MA / SPS	873	700	3.16	142	0.71	1.11	0.40	[86]
$Cu_{26}V_2Ge_6S_{32}$	MA / SPS	873	700	0.88	110	1.39	1.65	0.59	[78]
$Cu_{26}Cr_2Ge_6S_{32}$	MA / SPS	873	700	1.16	150	1.94	1.52	0.86	[78]
$Cu_{26}Mo_2Ge_6S_{32}$	MA / SPS	873	700	1.45	138	1.32	1.39	0.67	[78]
$Cu_{26}W_2Ge_6S_{32}$	MA / SPS	873	700	1.65	138	1.15	1.26	0.64	[78]
$[Cu_{26}Cr_2Ge_6]_{1.024}S_{32}$	MA / SPS	873	700	1.96	177	1.61	1.13	1.0	[101]

STS: Sealed-tube Synthesis; *CP*: Cold Press; *Ann.*: Annealing; *HP*: Hot Press; *MA*: Mechanical Alloying; *SPS*: Spark Plasma Sintering; * This work.

4.1. Pristine *A*-*E* colusites (*A* = V, Nb, Ta, Cr, Mo, W ; *E* = Ge, Sn)

In the first report of the low-temperature TE properties of the V-Sn colusite, the cold-pressed and sintered sample displayed a metallic behaviour with a resistivity and Seebeck coefficient values at room temperature of 0.4 mΩ cm and 27 µV K^{-1}, respectively (Table 4).[85] As a result of the consolidation route, the samples showed rather poor densities but retained an overall stoichiometry close to the nominal one thanks to the contained atmosphere of the silica tubes. However, the XRPD data clearly showed significant phase separation, probably arising from inhomogeneous repartition of the cations, as described in section 2.4. Nonetheless, these values were confirmed later by Bourgès *et al*. on mechanically alloyed samples sintered at low temperature, i.e. SPS at 873 K (sample L), with an electrical resistivity from *ca*. 0.4 mΩ cm to *ca*. 1.2 mΩ cm and a Seebeck coefficient from *ca*. 30 µV K^{-1} and *ca*. 90 µV K^{-1}, at 300 K and 675 K, respectively (Figure 11a, b).[86,89] Note that Bourgès et *al*. initially obtained a pristine sample containing 2 colusite phases,[86] and the measured performances were similar to those of the single phase ordered sample (Table 4).[89] The metallic behaviour of pristine V-Sn colusite is consistent with a measured charge carrier concentration of 3.26 × 10^{21} cm^{-3} and Hall mobility of 4.3 cm^2 V^{-1} s^{-1}.[89] The V-Sn colusite, phase-exsoluted or not,[86,89] with a composition close to the nominal stoichiometry of $Cu_{26}V_2Sn_6S_{32}$ and a high crystallinity with a low level of cationic disorder,[103] is metallic with low electrical resistivity and low Seebeck coefficient in agreement with the band structure calculations (Figure 5). These electrical transport properties lead to a power factor increasing from *ca*. 0.2 mW m^{-1} K^{-2} to *ca*. 0.7 mW m^{-1} K^{-2} at 300 K and 675 K, respectively (Figure 11c). In term of thermal transport properties, the pristine well-ordered V-Sn colusite, unlike its process-controlled counterpart, exhibits a fairly high thermal conductivity with values ranging from *ca*. 2.9 W m^{-1} K^{-1} to *ca*. 1.7 W m^{-1} K^{-1} at 300 K and 675 K, respectively (Figure 11d). In the first report of the low-temperature TE properties of the V-Sn colusite, the poorly densified (but stoichiometric w.r.t. sulphur loss) sample displayed a room temperature thermal conductivity of 2.7 W m^{-1} K^{-1}, consistent with the work of Bourgès *et al*. (Table 4).[85] This rather high thermal conductivity is the result of a combination of relatively high electronic contribution from the metallic behaviour of the electrical transport properties and high lattice contribution from the high level of cationic ordering (Figure 11e). Overall, the promising thermoelectric performances of V-Sn colusites are reflected in a reasonably high figure of merit for a sulphide with a ZT value reaching 0.27 at 675 K (Figure 11f).[89]

The isovalent substitution of vanadium by the other group 5 elements Nb and Ta successfully produced four new colusites with either Sn or Ge as *E* site cation (Table 4). This was first achieved by Kikuchi *et al*. with the synthesis of pristine Nb-Sn and Ta-Sn colusites.[92] However, the synthesis and sintering conditions point toward partially disordered samples with sulphur deficiency and cation

insertion, as described in section 2.4, so their electrical performances must be regarded as those of the process-controlled transport properties and will be discussed in section 4.2. Instead, in order to confirm that the performance of Nb-Sn and Ta-Sn are similar to those of V-Sn colusite, we measured the thermoelectric properties of samples prepared by mechanical alloying and low-temperature SPS (873 K, experimental procedure is detailed elsewhere).[93] As expected, when prepared in conditions that provide stoichiometric and well-ordered samples, Nb-Sn and Ta-Sn colusites exhibit strikingly similar transport properties to those of pristine V-Sn colusite (Figure 11). The minor differences, within the experimental error, between the V-Sn and the Nb/Ta-Sn colusites reported here are most likely caused by the different precursors used and the presence of trace amounts of impurities. These results clearly show that, in the case of group 5 Sn-colusite, the nature of the 2*a* cation has little impact on the electrical and thermal properties, in relation with weak cationic size difference and similar Pauling electronegativity for V^{5+}, Nb^{5+} and Ta^{5+} cations compared to group 6 colusite (see below). It is easily explained from the electronic and vibrational structures (section 3.1 and 3.2) of V-Sn colusite and the very minor role that V plays in the key regions, i.e. at the top of the valence band in the electronic structure and the low-frequency regions in the vibrational structure.

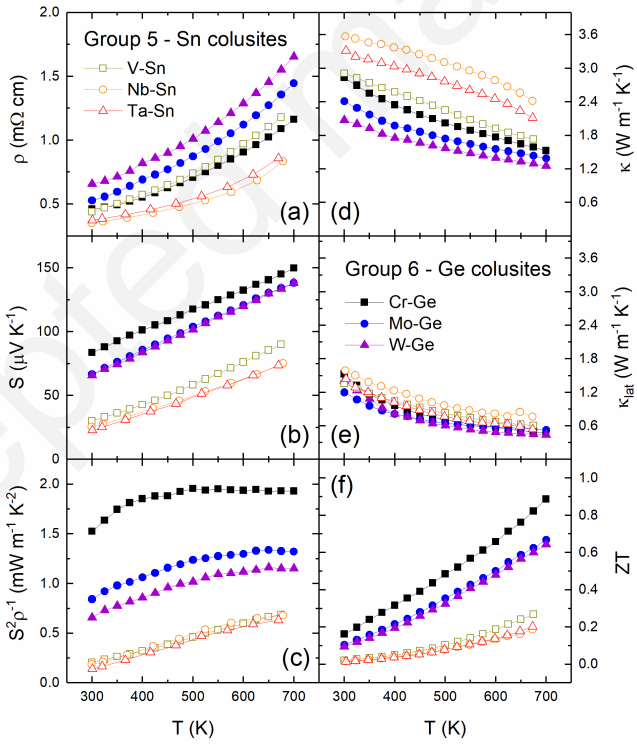

Fig. 11. Thermoelectric performance of selected stoichiometric *A-E* colusites with low level of temperature-induced cationic disorder including the (a) electrical resistivity, ρ, (b) Seebeck coefficient, S, (c) power factor, $S^2\rho^{-1}$, (d) thermal conductivity, κ, (e) lattice contribution to the thermal conductivity, κ_{lat}, and (f) the figure of merit, ZT. The graph includes original data for the Nb-

Sn and Ta-Sn colusites, data for the remaining compositions were taken and adapted from references [89] and [78].

The critical role of the "interstitial" 2*a* position was brought forward by the investigations into the transport properties of group 6 colusites, in particular with the study of the structure-property relationship in $Cu_{26}Cr_{2-x}A_xGe_6S_{32}$ (*A* = Mo, W; x = 0, 0.5, 1, 1.5, 2), detailed in section 4.4.[78,80] The specific structural characteristics of the mixed tetrahedral-octahedral complex can be found in section 2.3 and information about the electronic structure can be found in section 3.1. These are crucial to understand the excellent electrical performance of group 6 colusite in general, and of the Cr-Ge colusite in particular (Figure 11). First considering the pristine phases, it is remarkable to observe a low metallic electrical resistivity in Cr-Ge while this composition simultaneously exhibits the highest Seebeck coefficient, with values ranging from *ca*. 84 μV K^{-1} to *ca*. 150 μV K^{-1} for 300 K and 700 K, respectively (Figure 11a, b; Table 4). Comparatively, Mo-Ge and W-Ge colusites exhibit similar Seebeck coefficients with values ranging from *ca*. 65 μV K^{-1} to *ca*. 130 μV K^{-1} for 300 K and 700 K, respectively.[78] Note that all group 6 colusite samples were sintered at low temperature, i.e. SPS at 873 K, and HAADF-STEM images confirmed the overall good crystallinity of the samples and the absence of disordered regions or 1-D line defects. Calculations of the Seebeck coefficient using Boltzmann transport theory with a constant relaxation time approximation gave reasonably good agreement between experimental and theoretical results for Mo-Ge and W-Ge colusites, as well as V-Ge colusite prepared in similar conditions. The charge carrier concentration in the latter was measured to be *ca*. 6.3 × 10^{21} cm^{-3} at room temperature, decreasing down to *ca*. 4.2 × 10^{21} cm^{-3} and *ca*. 4.1 × 10^{21} cm^{-3} for Mo-Ge and W-Ge colusites respectively.[78] These results are well explained by standard models and the relationship between electrical conductivity, carrier concentration and Seebeck coefficient is respected. Indeed, the higher Seebeck coefficient and the lower electrical resistivity and charge carrier concentration in Mo-Ge and W-Ge colusites, compared to V-Ge colusite, are well explained by the change of oxidation states. Going from a group 5 to a group 6 "interstitial" cation shifts the Fermi level higher up in the valence band where fewer and heavier charge carriers contribute to the transport properties. However, in the case of Cr-Ge colusite, this standard model fails to reproduce the observed trend in the electrical transport properties.[78] While this approach explains the higher Seebeck coefficient and larger charge carrier effective mass in Cr-Ge, with calculations in fair agreement with the experiments, it fails to explain the lower electrical resistivity and higher charge carrier concentration. By considering the limits of the model, in particular the assumption that the relaxation time remains constant when substituting Cr^{6+} for Mo^{6+} or W^{6+}, Pavan Kumar *et al*. concluded that the nature of the *A* cation influences not only the crystal structure around the tetrahedral-octahedral $[AS_4]Cu_6$ complex, but also the relaxation time through its impact

on the Cu-S conductive network.[78] As described in section 2.2 and 2.3, the conductive network is less distorted and less electrostatically perturbed when replacing Mo^{6+} or W^{6+} by the smaller, less electronegative Cr^{6+}. Indeed, the *A*-Cu distance is shorter in Cr-Ge colusite, adding metallicity to the system with minimum disruption of the geometry of the conductive network. The authors experimentally linked this observation to an increase in the scattering relaxation time, τ, in the case of Cr-Ge colusite when combining calculated $\rho\tau$ and measured ρ.[78] Moreover, the relaxation time for Mo is slightly higher than for W, confirming the assumption that the nature of the *A* cation (size, induced distortions and Pauling electronegativity) influences the relaxation time and therefore the transport properties. Owing to the remarkable transport property behaviour in Cr-Ge colusite, the power factor is the highest reported to date for a iono-covalent sulphide with values ranging from 1.53 mW m^{-1} K^{-2} to 1.94 mW m^{-1} K^{-2} at 300 K and 700 K, respectively (Figure 11c).[78] In particular, the average power factor over this temperature range is exceptionally high with a value of 1.86 mW m^{-1} K^{-2}. This performance is particularly significant as thermoelectric sulphides usually reach high ZT values through ultralow thermal conductivity and modest power factor values. Note that ultralow thermal conductivity materials might even be unsuitable for a number of applications.[117]

As with the other well-ordered colusites, all the group 6-Ge colusites exhibit fairly high thermal conductivity values (Figure 11d; Table 4). For Cr-Ge colusite, the thermal conductivity decreases from *ca*. 2.8 W m^{-1} K^{-1} at 300 K to *ca*. 1.5 W m^{-1} K^{-1} at 700 K, consistent with the measured values for the ordered V-Sn colusite. For the Mo-Ge and W-Ge colusites, the thermal conductivity decreases progressively with the increasing atomic number.[78] As evidenced by the calculated lattice contributions to the thermal conductivity (Figure 11e), the difference between the three group 6 cations mostly depends on the electronic contribution. The lower electrical resistivity observed for the Cr-Ge colusite is thus responsible for its higher thermal conductivity. However, the corresponding record-high power factor more than makes up for this loss and the resulting figure of merit, *ZT*, reaches 0.86 at 700 K (Figure 11f). Comparatively, in the Mo-Ge and W-Ge colusites, despite a reduced thermal conductivity, the larger induced distortions of the conductive network caused by the size and higher electronegativity of the *A* cation yielded lower power factors and ultimately lower *ZT* values of *ca*. 0.1 and *ca*. 0.65 at 300 K and 700 K, respectively.[78] While the electronic contribution to the thermal conductivity is directly linked to the conductive network and thus might be difficult to reduce without altering the power factor, the lattice contribution however, remains high when compared to optimised group 5 colusites. The very similar lattice contributions between Cr-Ge, Mo-Ge and W-Ge colusites are consistent with their calculated vibrational structures (see section 3.2) where the *A* cation does not contribute significantly to the low frequency optic modes. Meanwhile, the important contribution from the neighbouring Cu positions, a feature shared

with V-Sn colusite, as well as Cu positions further away from the *A* cation, suggests that cationic disorder could have a similar impact on the vibrational structure, resulting in ultralow lattice thermal conductivity.

The electrical and thermal transport properties for the ordered pristine V-Ge colusite with no process-induced sulphur deficiency were reported by Pavan Kumar *et al*., with thermoelectric performances in between those of group 5 Sn- and group 6 Ge-colusites.[78] Once again, the transport properties behaviour is metallic with an electrical resistivity of 0.45 mΩ cm and a Seebeck coefficient of 45 μV K^{-1} at 300 K, up to *ca*. 0.9 mΩ cm and *ca*. 110 μV K^{-1} at 700 K, respectively (Table 4).[78] The moderate power factor of 0.4 mW m^{-1} K^{-2} at room temperature increases up to 1.4 mW m^{-1} K^{-2} at 700 K. This is promising for high temperature TE applications considering its excellent thermal stability (see section 5) and the non-optimised figure of merit, *ZT*, reaches 0.6 at 700 K.[78]

4.2. The role of process

The role of process over the level of cationic disorder and consequently over the transport properties has first been elucidated for the V-Sn colusite, following discrepancies in the reported performances.[89,93,103] This helped to explain the previously reported excellent performances of some other colusites, which can also be imputed to the effect of process. Indeed, most samples were prepared in high-temperature conditions, where sulphur volatilisation generates disorder and adjusts the charge carrier concentration. This was the case for the first report of the high-temperature TE performances of V-Sn and V-Ge colusites by Suekuni *et al*., using samples hot-pressed at 1073 K (Table 4).[88] The authors observed a more semiconducting behaviour compared to the metallic cold-pressed samples, as well as significantly larger unit cell parameters.[85] This was later confirmed by Bourgès *et al*. on single-phase samples by comparing mechanically alloyed V-Sn colusites sintered by either SPS at 873 K (sample L) or by hot pressing at 1023 K (sample H).[89] Both samples had very different transport behaviours, going from a metallic sample L to a less conducting sample H (Figure 12). Sample H exhibits an electrical resistivity from *ca*. 2.8 mΩ cm to *ca*. 4.3 mΩ cm and a Seebeck coefficient from *ca*. 100 μV K^{-1} and *ca*. 175 μV K^{-1}, at 300 K and 675 K, respectively, with an upturn in the electrical resistivity at around 350 K (Figure 12a, b). The larger sulphur volatilisation decreases the measured charge carrier concentration from 3.26×10^{21} cm^{-3} to 1.35×10^{21} cm^{-3} and the Hall mobility from 4.3 cm^2 V^{-1} s^{-1} to 2.1 cm^2 V^{-1} s^{-1} for samples L and H, respectively.[89] Variations in the electrical transport properties are mainly encouraged by sulphur volatilisation and cationic rearrangement, in particular with potential Cu intercalation.[99] Overall, the power factor of the process-controlled V-Sn colusite ranges from *ca*. 0.4 mW m^{-1} K^{-2} at 300 K to *ca*. 0.7 mW m^{-1} K^{-2} at 675 K (Figure 12c).[89] This represents a two-fold increase at room temperature up

to a value at 675 K similar to that of the well-ordered V-Sn colusite. Similarly, comparing the TE performance of V-Ge colusites sintered at different temperatures, the Seebeck coefficient of V-Ge hot-pressed at 1073 K[88] reached much higher values than the cold-pressed[85] or SPS (873 K) samples[78] with a room temperature value of 125 μV K^{-1} up to 215 μV K^{-1} at 663 K (Table 4).[88] Simultaneously, the resistivity increased by more than an order of magnitude despite the higher density of the hot-pressed sample. Note that owing to the isovalent substitution of Sn^{4+} by Ge^{4+} and the insignificant contribution of these atoms to the top of the valence band, V-Ge colusite displays electrical transport properties remarkably similar to the V-Sn colusite when prepared in similar conditions, i.e. at a high sintering temperature of 1073 K (Table 4).

The thermal conductivity of V-Sn colusite hot-pressed at 1023 K (sample H) is significantly lowered w.r.t. sample L from *ca*. 2.9 W m^{-1} K^{-1} to 0.67 W m^{-1} K^{-1} at 300 K and from *ca*. 1.7 W m^{-1} K^{-1} to 0.56 W m^{-1} K^{-1} at 675 K (Figure 12d). Such low thermal conductivity is consistent with the sulphur-deficient high-temperature hot-pressed sample reported by Suekuni *et al*. (Table 4).[88] The decrease in the thermal conductivity with increased sintering temperature arises from reductions in both electronic and lattice contributions (Figure 12e). In particular, the decrease in the lattice contribution is significant with high-temperature hot-pressed samples exhibiting a quasi-glassy thermal conductivity, down to the theoretical minimum of 0.27 W m^{-1} K^{-1}.[89,118] At low temperature, sample H even exhibits a glass-like temperature dependence of the lattice thermal conductivity.[103] The significant decrease in both contributions to the thermal conductivity is attributed to short-wavelength phonon scattering by S vacancies[99] and cationic disorder.[89,103] This conclusion was supported by a decrease in measured sound velocities (Table 2) and the shape of the phonon dispersion and vibrational DOS described in section 3.2 (Figure 5). However, further insights on the impact of the Cu-Sn antisites, described by Candolfi *et al*.[103] (see section 3.3) strongly suggest that the distribution of cations is significantly modified with temperature and has a more significant impact on the transport properties, along with potential Cu intercalation. In other words, the fully disordered regions observed in section 3.3, where symmetry is lost, are less responsible for variations in thermal transport properties than antisite defects. The glasslike temperature dependence of the lattice thermal conductivity is thus caused by a shortening of the acoustic phonon lifetimes, encouraged by mixed occupation on the cationic sites, most likely in the form of Cu-Sn antisites, as evidenced by their low formation energy (Table 3). As a result, the figure of merit of samples presenting a high degree of cationic disorder is significantly improved by the glasslike lattice contribution to the thermal conductivity. The disordered V-Sn colusite sintered at high-temperature (sample H) reaches a ZT of 0.93 at 673 K which constitutes a three-fold improvement over the more stoichiometric and more ordered colusite sintered at 873 K.[89] Similarly, the thermal conductivity measured in the V-Ge

colusite sintered at high temperature is very low with values close those of disordered V-Sn colusites. As a result, the figure of merit of V-Ge colusite ranged from 0.26 to 0.73 at 350 K and 663 K, respectively.[88] Moreover, in the same study with a sintering temperature of 1073 K, the V-Sn colusite displayed slightly lower performances, suggesting that process-controlled V-Ge colusite might also be a highly promising thermoelectric sulphide.

Note that a power factor of 1.04 mW m^{-1} K^{-2} at 663 K was achieved for an up-scaled sample after SPS sintering at 1083 K (Table 4).[93] In the latter, the formation of structural defects that differ from the lab-scale high-purity precursors synthesis (see section 3.3) are responsible for its different transport properties. In particular, the charge carrier concentration was measured to be much higher, $n_{h+} \approx 4.5 \times 10^{21}$ cm^{-3}, with slightly lower charge carrier mobility, $\mu_{300K} \approx 1.4$ cm^2 V^{-1} s^{-1}.[93] The thermal conductivity remained higher than those of the lab-scale high-purity samples, evidencing a competition of effects between the various types of process-controlled defects described in section 3.3. Because both electrical conductivity and lattice thermal conductivity remained comparatively high, the overall thermal conductivity was measured to be twice as high as sample H. Owing to the record high power factor in this material, the figure of merit remained fairly high, reaching *ca*. 0.7 at 673 K and an average value of 0.41 over the temperature range $300 \leq T / K \leq 673$.[93]

As expected from the effect of process of the TE properties of V-Sn colusite, a very similar scenario was confirmed with the other group 5 cations by comparing the performances of Nb-Sn and Ta-Sn colusites hot-pressed at 1023 K, from the work of Kikuchi *et al*.,[92] with samples sintered by SPS at 873 K (Figure 12).[89] Indeed, the electrical resistivity of the materials hot-pressed at high temperature ranges from *ca*. 3.7 mΩ cm and 2.6 mΩ cm at 300 K to *ca*. 7.3 mΩ cm and 5.7 mΩ cm at 660 K for Nb-Sn and Ta-Sn colusites, respectively (Figure 12a). The large increase in electrical resistivity caused by the higher sintering temperature is strikingly similar to the one observed for V-Sn colusite. The same can be said about the Seebeck coefficient with values ranging from *ca*. 120 µV K^{-1} at 300 K to *ca*. 200 µV K^{-1} at 660 K for both Nb-Sn and Ta-Sn colusites (Figure 12b).[92] The maximum power factor was achieved for the Ta-Sn sample with values ranging from *ca*. 0.5 mW m^{-1} K^{-2} at 300 K to *ca*. 0.7 mW m^{-1} K^{-2} at 675 K (Figure 12c). By analogy with V-Sn colusites, the decrease in both electronic and lattice contributions to the thermal conductivity are most likely caused by an increased level of process-induced cationic disorder. As a result, the figure of merit is well optimised, reaching *ca*. 0.8 for Ta-Sn colusite at 670 K.[92]

Similarly, the TE properties of Nb-Ge and Ta-Ge colusites have been reported for samples prepared using high sintering temperatures, thus producing process-induced sulphur-deficient samples with a less metallic behaviour than the stoichiometric Sn-colusite counterparts presented in section 4.1.[97]

Considering this, they displayed thermoelectric properties similar to those of their Sn-containing counterparts when sintered in similar conditions (Table 4). By analogy with what we observed in Sn-colusites (Figure 12), we can speculate that pristine Nb-Ge and Ta-Ge colusites should have a very metallic behaviour close to that of group 5-Sn colusites. It is very likely that their excellent performances were achieved by process-controlled sulphur volatilisation and cationic disordering. In particular, the Nb-Ge colusite exhibits ZT values between *ca*. 0.2 and *ca*. 1 at 300 K and 670 K, respectively.[97]

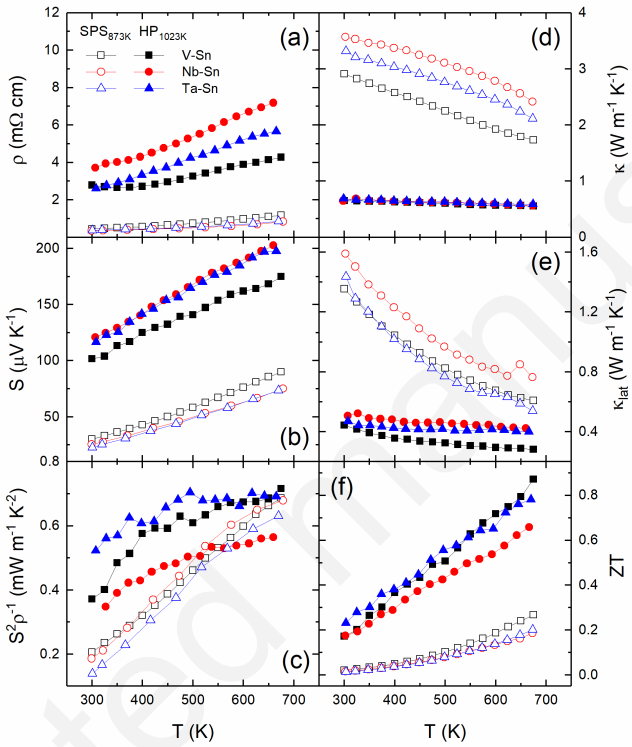

Fig. 12. Thermoelectric performance of selected *A-E* colusites, prepared by SPS at 873 K and hot press (HP) at 1023 K, showing the effect of temperature-induced cationic disorder including the (a) electrical resistivity, ρ, (b) Seebeck coefficient, S, (c) power factor, $S^2\rho^{-1}$, (d) thermal conductivity, κ, (e) lattice contribution to the thermal conductivity, κ_{lat}, and (f) the figure of merit, ZT. The graph included original data for the Nb-Sn and Ta-Sn colusites, data for the remaining compositions were taken and adapted from references [89] and [92].

Introducing cationic disorder in order to reduce the lattice thermal conductivity has been considered for the high power factor Cr-Ge colusite. However, the required high temperatures are impractical due its lower thermal stability, see section 5.[115] Artificially increasing the cationic disorder by using cationic overstoichiometry has led to a disruption of the electrical transport properties, with a more pronounced effect on the electronic contribution to the thermal conductivity via tuning of the charge carrier concentration.[101] With only a small fraction of additional cations, $[Cu_{26}Cr_2Ge_6]_{1.024}S_{32}$, a

distortion of the conductive network, similar to that of solid solutions detailed in section 4.4, could be achieved, resulting in an ionised impurity-like scattering mechanism above 100 K. This time however, the charge carrier concentration is simultaneously decreased, leading to higher values for the Seebeck coefficient and an overall power factor remaining fairly high while decreasing the electrical component to the thermal conductivity (Table 4).[101] Unfortunately, as opposed to temperature-induced disorder, this strategy does not seem to increase the concentration of antisite defects responsible for shorter acoustic phonon lifetimes, and thus the lattice contribution to the thermal conductivity remains almost the same. The best performing composition, $[Cu_{26}Cr_2Ge_6]_{1.024}S_{32}$, still exhibits a minor improvement with ZT reaching the unity at 700 K.[101]

4.3. Doping strategies

Initially, partial substitution of Cu by Zn was first proposed as a doping strategy with the added benefit of producing single-phase materials in the early reports (section 2.4).[85,86] The substitution of Cu by a divalent element enables tuning of the carrier concentration by filling the valence band up to a semiconducting behaviour where the formal charges can be written as $[Cu^+]_{22}[Zn^{2+}]_4[V^{5+}]_2[Sn^{4+}/Ge^{4+}]_6[S^{2-}]_{32}$. This lead to a significant increase in the electrical resistivity and Seebeck coefficient for Zn-doped V-Sn and V-Ge colusites at 300 K, respectively (Table 4).[85] However, the power factor at high temperature was only optimised by Zn doping on samples sintered at low temperature (Figure 13c),[86] i.e. on samples that remained rather stoichiometric and relatively free of defects. In those samples, the electrical resistivity and Seebeck coefficient were significantly increased with the sintering temperature, as exemplified by $Cu_{24}Zn_2V_2Sn_6S_{32}$ (Figure 13).[86,87] The best value was achieved by $Cu_{25}ZnV_2Sn_6S_{32}$ sintered at 873 K with 0.92 mW m^{-1} K^{-2} at 700 K (Table 4).[86] For samples sintered at higher temperature, and thus exhibiting a more semiconducting behaviour, Zn doping was found to be detrimental for the electrical properties, as with $Cu_{24}Zn_2V_2Sn_6S_{32}$ hot-pressed at 1073 K (Figure 13).[87]

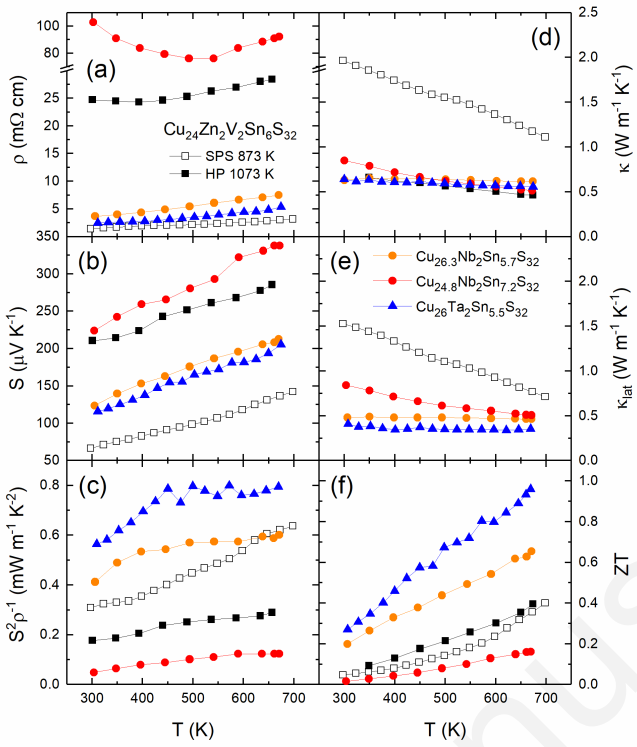

Fig. 13. Thermoelectric performance of $Cu_{24}Zn_2V_2Sn_6S_{32}$, $Cu_{26-x}Nb_2Sn_{6+x}S_{32}$ (x = -0.3, 1.2) and $Cu_{26}Ta_2Sn_{5.5}S_{32}$ including the (a) electrical resistivity, ρ, (b) Seebeck coefficient, S, (c) power factor, $S^2\rho^{-1}$, (d) thermal conductivity, κ, (e) lattice contribution to the thermal conductivity, κ_{lat}, and (f) the figure of merit, ZT. Data were taken and adapted from references [86,87,97,99].

Adding extra cations in the form of Co, Ni and Fe insertion was attempted, with little-to-no effect on the unit cell parameters and thermoelectric properties.[100] It seems however that, in the case of Fe addition, the large increase in electrical resistivity, consistent with the observed decrease in charge carrier concentration and mobility, evidence some level of substitution. Bouyrie *et al*.[102] studied the possible substitution of Cu by Ni and Co in V-Ge colusite as such strategy was found to be effective in the related tetrahedrites.[102] While Co substitution does seem to behave in a similar fashion than Zn, resulting in a loss of thermoelectric performance, Ni substitution appears to be more complicated with retention of the metallic character of the electrical resistivity while the Seebeck coefficient remains comparatively low. As a result, both doping strategies were found to be rather ineffective for thermoelectric performance enhancement.

Bouyrie *et al*. proposed to use *E*-site off-stoichiometry in order to tune the TE performance of Nb/Ta-Sn and Nb/Ta-Ge colusites.[97] The aim of producing samples with Sn or Ge-deficiency is two-fold; it allows for charge carrier concentration adjustments and, in the cases of Ta-Ge colusite, helps to produce phase-pure materials, probably by preventing the formation of a disordered phase in regions with high Ge/Cu ratio. Again, note that the reported transport properties are best described

as those of the sulphur-deficient, partially disordered phases. They obtained samples with generally better purity and no, or less, second phases by synthesising *E*-site cation deficient samples. The electrical performance for Sn-deficient samples clearly show a lower electrical resistivity for an unchanged Seebeck coefficient w.r.t. the pristine phases, resulting in the highest power factor values achieved in Nb/Ta colusites (Table 4). As presented in section 2.4 and 3.3, Suekuni *et al*. relied on earlier findings on the defects chemistry of the V-Sn colusite, and in particular on their dependence on composition and preparation conditions, in order to boost the thermoelectric performance of the parent Nb-Sn colusite.[99] The authors confronted the effect of varying Sn:Cu ratio and structural disorder, illustrated here in Figure 13 by opposing the performance of $Cu_{26-x}Nb_2Sn_{6+x}S_{32}$ for x = -0.3, hot-pressed at 873 K and 973 K (Table 4), and for x = 1.2, corresponding to a sample with complete loss of cationic ordering (see section 3.3). As expected, increasing the Cu:Sn ratio has led to a decrease in the electrical resistivity and Seebeck coefficient (Figure 13a, b), consistent with the work of Bouyrie *et al*.[97]. Meanwhile, increasing the sintering temperature of $Cu_{26.3}Nb_2Sn_{5.7}S_{32}$ has led to a noticeable decrease in charge carrier concentration, evidenced by a four-fold increase in the electrical resistivity over the whole investigated temperature range (Table 4).[99] This is accompanied by nearly twice higher Seebeck coefficient and an improved power factor over the whole temperature range.[99] For the fully disordered $Cu_{24.8}Nb_2Sn_{7.2}S_{32}$, the electrical resistivity is increased by more than an order of magnitude with a temperature dependence at the frontier between semiconducting and metallic (Figure 13a). The Seebeck coefficient is also largely increased with values ranging from *ca*. 225 µV K^{-1} and *ca*. 350 µV K^{-1} at 300 K and 675 K, respectively (Figure 13b). This apparent decrease in the charge carrier concentration is consistent with a loss of the mixed valence of Cu, as it is the case with Zn substitution in V-Sn colusite.[86]

The thermal conductivity for all Nb/Ta-Ge/Sn colusites and their doped-derivatives remains below 0.7 W m^{-1} K^{-1} over the whole temperature range, when prepared at high sintering temperature (Figure 13d; Table 4). This highlights the importance of process over stoichiometric changes when attempting to decrease the thermal conductivity.[92,97] It is likely that the thermal conductivity for the corresponding samples sintered in milder conditions would exhibit higher values, more consistent with those of the well-ordered V-Sn colusite, sample L (Figure 12d, e). Overall, process-enhanced $Cu_{26}Ta_2Sn_{5.5}S_{32}$ exhibits similar performances than the pristine Nb-Ge colusite with a figure of merit reaching around unity at 670 K.[97] The case of the fully disordered $Cu_{24.8}Nb_2Sn_{7.2}S_{32}$ is intriguing as its lattice contribution to the thermal conductivity is almost identical than those of Nb/Ta-Sn colusite sintered in similar conditions (Figure 13d, e). Despite an increased level of disorder and a complete loss symmetry elements responsible of the colusite structure, $Cu_{24.8}Nb_2Sn_{7.2}S_{32}$ exhibits a lattice thermal conductivity from 0.84 W m^{-1} K^{-1} at 300 K to 0.51 W m^{-1} K^{-1} at 673 K (Figure 13e).[99] This is

consistent with the work of Candolfi *et al*. in the V-Sn colusite system, where the large decrease in the lattice contribution to the thermal conductivity upon increasing the sintering temperature could be mostly attributed to the formation of Cu-Sn antisite defects.[103] The fully disordered regions observed in section 3.3, compared to the modified ordered structure of $Cu_{26.3}Nb_2Sn_{5.7}S_{32}$, were ineffective in reducing the thermal conductivity. This supports the conclusion drawn by Candolfi *et al*. that the atomic-scale defects in a modified ordered structure, rather than disordered regions, are likely to provide additional phonon scattering.[103]

4.4. Solid-solutions

As opposed to chemical doping and its predictable impact on transport properties, forming solid-solutions in *A*-Ge colusites was successful on a more fundamental level. While they were found rather ineffective in improving the TE performances of group 6-Ge colusites, the Cr/Mo and Cr/W solid solutions confirmed the crucial role of Cr within the tetrahedra-octahedral complex in the conductive mechanism of Ge-based colusites.[80] While the Seebeck coefficient follows the expected trend with values very similar to those of the pristine Cr-Ge colusite, consistent with the very similar measured charge carrier concentration, the electrical resistivity shows an upturn at a temperature of *ca*. 375 K, below which the resistivity exhibits a semiconducting behaviour. This is confirmed by low temperature transport properties measurements (Figure 14). As with Cr-Ge colusite (see section 4.1), theoretical calculations within the constant relaxation time approximation cannot account for this observation.[80] Similarly, combining calculated $\rho\tau$ and measured ρ for solid solutions are consistent with pristine materials above the upturn temperature but the determined relaxation time suffers significant shortening when the temperature decreases below 400 K. This underlines the importance of Cr in 2*a* position but also the role of chemical disorder within the tetrahedral-octahedral complex, induced by the mixed occupancy by atoms of largely different ionic radii and illustrated by the cation-size variance, σ^2.[119]

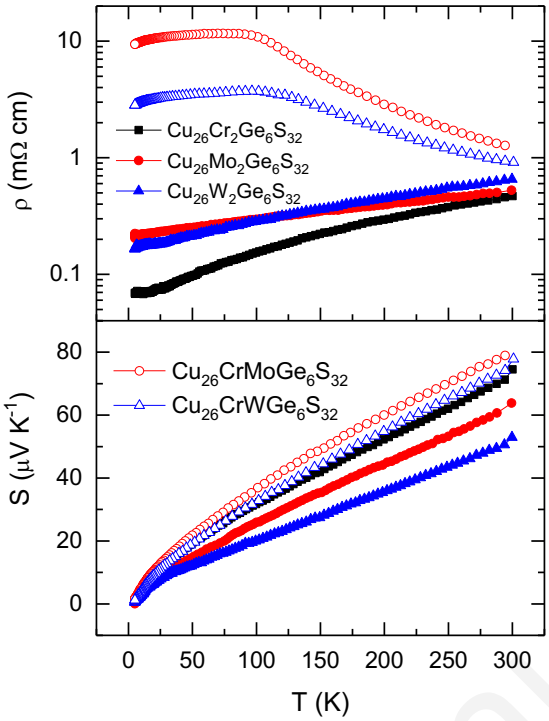

Fig. 14. Electrical resistivity, *ρ*, and Seebeck coefficient, *S*, of pristine group 6 colusites and Cr/Mo and Cr/W solid solutions at low temperature. Data were taken and adapted from reference [80].

The effect of cation-size mismatch is particularly clear when looking at the low temperature electrical resistivity and Hall mobility measurements (Figure 15). For samples with the highest cation-size variance, i.e. for a 50/50 occupation of the 2*a* "interstitial site", the conduction mechanism above 100 K changes from a typical acoustic phonon scattering (Hall mobility $\propto T^{-3/2}$) in pristine colusites to an ionised impurity-like scattering (Hall mobility $\propto T^{3/2}$).[80] Pavan Kumar *et al*. suggested that this behaviour originates from phenomena associated with variable-range hopping (VRH) and/or chemical disorder/localisation. In any case, these results demonstrated the (often overlooked) importance of cation-size mismatch in solid solutions, in particular when the associated chemical disorder indirectly influences the electrical transport properties through distortions in the conductive network. The evolution of the thermal conductivity in the solid solutions is consistent with the evolution of the cation-size variance as the Cr/Mo and Cr/W solid-solutions show lower values than the corresponding pristine phases. This mainly originates from the increase in the electrical resistivity, maximised for the highest cation-size variance. Because the power factor had been significantly decreased by the perturbations on the conductive network, the lower thermal conductivity achieved in the solid solutions with the highest cation-size variance only compensates for the loss, with ZT remaining around 0.9 at 700 K.[80]

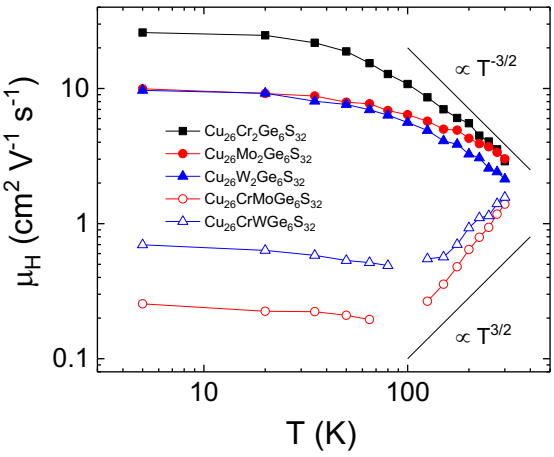

Fig. 15. Hall mobility as a function of temperature for pristine group 6 colusites and Cr/Mo and Cr/W solid solutions. Data were taken and adapted from reference [80].

5. Stability and scalability

The excellent performances in processed-controlled, cost-efficient V-Sn colusite, $Cu_{26}V_2Sn_6S_{32}$, and in high power factor Cr-Ge colusite, $Cu_{26}Cr_2Ge_6S_{32}$, have led researchers to consider stability and scalability issues for practical purposes. An extensive investigation of the thermal stability of Cr-Ge colusite was carried out by Lemoine *et al*., with the combined objectives of defining the stability range for Cr-Ge colusite and exploring the possibility to induce process-controlled cationic disorder during sintering.[115] Using differential scanning calorimetry (DSC), thermogravimetric analysis (TGA), X-ray powder diffraction (XRPD) and temperature-dependent neutron powder diffraction (NPD), the authors determined that Cr-Ge colusite was highly stable up to at least 700 K. Cycled electrical property measurements up to 700 K, including Seebeck coefficient and electrical resistivity, show no sign of degradation of the power factor.[115] However, superficial sulphur loss occurs above 760 K and decomposition of the colusite phase begins above 830 K with full decomposition above 930 K. Cycling electrical property measurements at a maximum temperature of 760 K clearly show a steady decrease of the charge carrier concentration caused by sulphur loss. Comparatively, while Cr-Ge colusite decomposes into ternary Cu-Ge-S and Cu-Cr-S phases in two steps at 830 K and 880 K, the vanadium counterpart, $Cu_{26}V_2Ge_6S_{32}$, shows no sign of degradation and appears stable up to at least 1000 K.[115] The lower temperature stability of Cr-Ge colusite is explained by the presence of Cr^{6+} in tetrahedral sulphur environment, a structural feature observed, to the best of our knowledge, only in synthetic Cr-Ge colusite.[78] The limited thermal stability of the Cr-Ge colusite results in difficulties in obtaining process-controlled disorder by increasing the sintering temperature. An ultralow lattice contribution to the thermal conductivity, such as those observed in disordered group 5 colusites,

combined with the particularly high power factor of Cr-Ge colusite would result in ZT values well above the unity.

In term of scalability, the feasibility of mechanochemical synthesis has been demonstrated for many sulphides and this choice of synthetic route is justified by its relatively easy application on a large scale.[120] As mentioned in the previous sections, the V-Sn colusite can be produced in relatively large batches, 200 g per milling cycle, using industrial grade precursors.[93] An in-depth investigation of the large scale sintering of large monoliths of V-Sn colusite in currently ongoing. Finally, the production of industrial grade V-Sn colusite was recently achieved in an industrial eccentric vibratory ball mill.[121]

Finally, with the aim to consider colusites as *p*-type materials in thermoelectric devices, the determination of their mechanical properties is also an important point which was considered only by Bourgès *et al*. on V-Sn colusite.[86] Chetty *et al*. reported the preparation and performances of a single thermoelectric element based on colusite $Cu_{26}Nb_2Ge_6S_{32}$.[122] An Au metal layer was demonstrated to be a successful diffusion barrier, preventing Cu diffusion and ensuring a low specific contact resistance of 4-5 × 10^{-10} Ω m^2.[122] The maximum conversion efficiency of this single element was estimated to be ≈ 3.3 % for a temperature gradient of 273 K (hot-side and cold-site kept at 570 K and 297 K, respectively), for a predicted maximum of ≈ 4.5 %.[122]

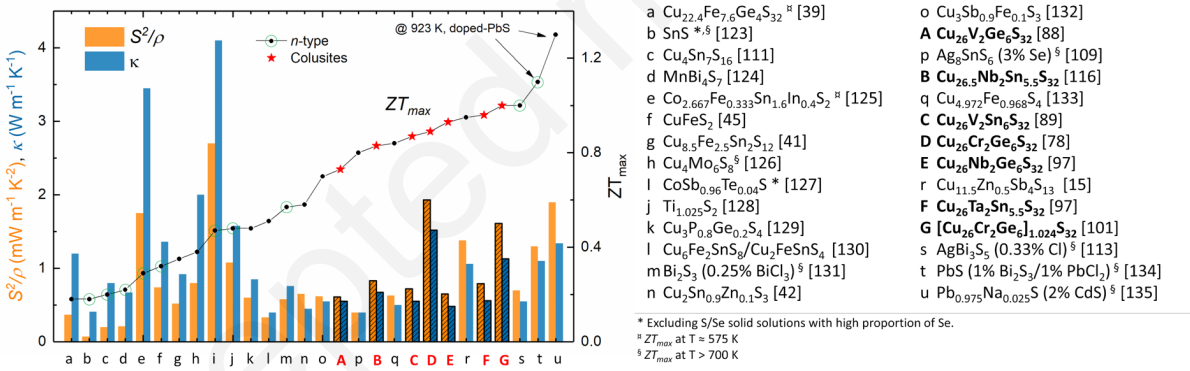

Fig. 16. Comparison between selected colusite materials and state-of-the-art sulphides including the power factor, S^2/ρ,(orange bars) and the thermal conductivity, κ, (blue bars) at the temperature at which the figure of merit reaches its maximum value, ZT_{max}, (scatters). Unless indicated otherwise, these performances are achieved at temperatures between 600 K and 700 K.

6. Concluding remarks and future prospects

Synthetic derivatives of the natural quaternary sulphide colusite have only been studied since 2014, though reaching thermoelectric performances on par with current state-of-the-art sulphides (Figure 16). The cousin material tetrahedrite, incidentally identified as an excellent thermoelectric by the same research group 2 years earlier than colusite,[13] has comparatively attracted significantly more

attention. However, in a short time and comparatively fewer articles, colusite now exhibits similar thermoelectric performances. It is worth mentioning that, despite the absence of comparative studies of the mechanical properties between these two families of materials, it is generally accepted that colusite samples, when mechanically alloyed, are significantly less brittle and easier to cut. It is possible that colusite suffered from the early competition of tetrahedrite and possibly influenced by its failed industrial experience. One critical factor against colusite is the extreme scarcity of natural samples that undoubtedly excludes the use of re-processed natural minerals, as it was suggested for the earth-abundant tetrahedrite and bornite.[36,136] Nonetheless, we can be hopeful about the future of colusite with much remaining to be investigated, in particular with the prospects of combining the two successful approaches, process-controlled disorder and functionalisation of the conductive network. With this review, we hope that the peculiar transport properties of colusites will pique the interest of scientists inside and outside the thermoelectric community.

7. Acknowledgements

This work was supported by the French Agence Nationale de la Recherche (ANR) through the programs Energy Challenge for Secure, Clean and Efficient Energy (Challenge 2, 2015, ANR-15-CE05-0027) and FEDER and Normandy Region. The authors would like to thank Christophe Candolfi, Koichiro Suekuni, Rabih Al Rahal Al Orabi and Marco Fornari for their useful input and discussions.

8. Note

† Translated from French « Les réunions des substances thermo-électriques citées précédemment sont celles qui, étant produites artificiellement, donnent les effets les plus énergiques. Peut-être irait-on au-delà avec des minéraux naturels ; (…) » [48]

9. References

1 D. Beretta, N. Neophytou, J. M. Hodges, M. G. Kanatzidis, D. Narducci, M. Martin- Gonzalez, M. Beekman, B. Balke, G. Cerretti, W. Tremel, A. Zevalkink, A. I. Hofmann, C. Müller, B. Dörling, M. Campoy-Quiles and M. Caironi, *Mater. Sci. Eng. R Reports*, 2019, **138**, 100501.

2 R. Freer and A. V Powell, *J. Mater. Chem. C*, 2020, **8**, 441–463.

3 D. Champier, *Energy Convers. Manag.*, 2017, **140**, 167–181.

4 J. R. Sootsman, D. Y. Chung and M. G. Kanatzidis, *Angew. Chemie - Int. Ed.*, 2009, **48**, 8616–8639.

5 J. He and T. M. Tritt, *Science (80-.).*, 2017, **357**, eaak9997.

6 X.-L. Shi, J. Zou and Z.-G. Chen, *Chem. Rev.*, 2020, **120**, 7399–7515.

7 A. V Powell, *J. Appl. Phys.*, 2019, **126**, 100901.

8 D. Bernhardt (U.S. Department of the Interior) and J. F. Reilly II (U.S. Geological Survey), *Mineral Commodity Summaries*, 2020.

9 X. Lu and D. T. Morelli, *MRS Commun.*, 2013, **3**, 129–133.

10 P. Wyżga, M. Bobnar, C. Hennig, A. Leithe-Jasper, T. Mori and R. Gumeniuk, *Zeitschrift für Anorg. und Allg. Chemie*, 2017, **643**, 858–863.

11 P. Zhang, Y.-X. Zhang, H. Lai, J. Deng, J. Feng and Z.-H. Ge, *Mater. Lett.*, 2019, **253**, 430–433.

12 H. Xie, X. Su, G. Zheng, T. Zhu, K. Yin, Y. Yan, C. Uher, M. G. Kanatzidis and X. Tang, *Adv. Energy Mater.*, 2017, **7**, 1–14.

13 K. Suekuni, K. Tsuruta, T. Ariga and M. Koyano, *Appl. Phys. Express*, 2012, **5**, 2–5.

14 R. Chetty, A. Bali and R. C. Mallik, *J. Mater. Chem. C*, 2015, **3**, 12364–12378.

15 X. Lu, D. T. Morelli, Y. Xia, F. Zhou, V. Ozolins, H. Chi, X. Zhou and C. Uher, *Adv. Energy Mater.*, 2013, **3**, 342–348.

16 K. Suekuni, K. Tsuruta, M. Kunii, H. Nishiate, E. Nishibori, S. Maki, M. Ohta, A. Yamamoto and M. Koyano, *J. Appl. Phys.*, 2013, **113**, 043712.

17 Y. Bouyrie, C. Candolfi, V. Ohorodniichuk, B. Malaman, A. Dauscher, J. Tobola and B. Lenoir, *J. Mater. Chem. C*, 2015, **3**, 10476–10487.

18 T. Barbier, P. Lemoine, S. Gascoin, O. I. Lebedev, A. Kaltzoglou, P. Vaqueiro, A. V. Powell, R. I. Smith and E. Guilmeau, *J. Alloys Compd.*, 2015, **634**, 253–262.

19 T. Barbier, S. Rollin-Martinet, P. Lemoine, F. Gascoin, A. Kaltzoglou, P. Vaqueiro, A. V. Powell and E. Guilmeau, *J. Am. Ceram. Soc.*, 2016, **99**, 51–56.

20 A. P. Gonçalves and E. B. Lopes, *Semiconductors*, 2019, **53**, 1817–1824.

21 K. Suekuni and T. Takabatake, *APL Mater.*, 2016, **4**, 104503.

22 A. V Powell and P. Vaqueiro, in *Thermoelectric Materials and Devices*, The Royal Society of Chemistry, 2017, pp. 27–59.

23 S. Il Kim, K. H. Lee, H. A. Mun, H. S. Kim, S. W. Hwang, J. W. Roh, D. J. Yang, W. H. Shin, X. S. Li, Y. H. Lee, G. J. Snyder and S. W. Kim, *Science (80-.).*, 2015, **348**, 109–114.

24 X. Lu, Q. Zhang, J. Liao, H. Chen, Y. Fan, J. Xing, S. Gu, J. Huang, J. Ma, J. Wang, L. Wang and W. Jiang, *Adv. Energy Mater.*, 2020, **10**, 1902986.

25 Y. Liu, L.-D. Zhao, Y. Zhu, Y. Liu, F. Li, M. Yu, D.-B. Liu, W. Xu, Y.-H. Lin and C.-W. Nan, *Adv. Energy Mater.*, 2016, **6**, 1502423.

26 P. Vaqueiro, G. Guélou, M. Stec, E. Guilmeau and A. V. Powell, *J. Mater. Chem. A*, 2013, **1**, 520–523.

27 L. D. Zhao, D. Berardan, Y. L. Pei, C. Byl, L. Pinsard-Gaudart and N. Dragoe, *Appl. Phys. Lett.*, 2010, **97**, 92118.

28 J.-A. Dolyniuk, B. Owens-Baird, J. Wang, J. V Zaikina and K. Kovnir, *Mater. Sci. Eng. R Reports*, 2016, **108**, 1–46.

29 J. Wang, Y. He, N. E. Mordvinova, O. I. Lebedev and K. Kovnir, *Chem*, 2018, **4**, 1465–1475.

30 X. Shi, J. Yang, J. R. Salvador, M. Chi, J. Y. Cho, H. Wang, S. Bai, J. Yang, W. Zhang and L. Chen, *J. Am. Chem. Soc.*, 2011, **133**, 7837–7846.

31 D. Qin, B. Cui, L. Yin, X. Zhao, Q. Zhang, J. Cao, W. Cai and J. Sui, *ACS Appl. Mater. Interfaces*, 2019, **11**, 25133–25139.

32 S. M. Kauzlarich, A. Zevalkink, E. Toberer and G. J. Snyder, in *Thermoelectric Materials and Devices*, The Royal Society of Chemistry, 2017, vol. 2017-Janua, pp. 1–26.

33 S. Ohno, K. Imasato, S. Anand, H. Tamaki, S. D. Kang, P. Gorai, H. K. Sato, E. S. Toberer, T. Kanno and G. J. Snyder, *Joule*, 2018, **2**, 141–154.

34 A. Nozariasbmarz, A. Agarwal, Z. A. Coutant, M. J. Hall, J. Liu, R. Liu, A. Malhotra, P. Norouzzadeh, M. C. Öztürk, V. P. Ramesh, Y. Sargolzaeiaval, F. Suarez and D. Vashaee, *Jpn. J. Appl. Phys.*, 2017, **56**, 05DA04.

35 N. Seltenrich, Thermoelectrics: An old, new tech, https://engineering.berkeley.edu/news/2016/05/thermoelectrics-an-old-new-tech/, (accessed 6 October 2020).

36 P. Qiu, T. Zhang, Y. Qiu, X. Shi and L. Chen, *Energy Environ. Sci.*, 2014, **7**, 4000–4006.

37 G. Guélou, A. V. Powell and P. Vaqueiro, *J. Mater. Chem. C*, 2015, **3**, 10624–10629.

38 V. Pavan Kumar, T. Barbier, P. Lemoine, B. Raveau, V. Nassif and E. Guilmeau, *Dalt. Trans.*, 2017, **46**, 2174–2183.

39 V. Pavan Kumar, L. Paradis-Fortin, P. Lemoine, V. Caignaert, B. Raveau, B. Malaman, G. Le Caër, S. Cordier and E. Guilmeau, *Inorg. Chem.*, 2017, **56**, 13376–13381.

40 V. Pavan Kumar, L. Paradis-Fortin, P. Lemoine, G. Le Caer, B. Malaman, P. Boullay, B. Raveau, G. Guélou and E. Guilmeau, *ACS Appl. Energy Mater.*, 2019, **2**, 7679–7689.

41 V. Pavan Kumar, T. Barbier, V. Caignaert, B. Raveau, R. Daou, B. Malaman, G. Le Caër, P. Lemoine and E. Guilmeau, *J. Phys. Chem. C*, 2017, **121**, 16454–16461.

42 Y. Shen, C. Li, R. Huang, R. Tian, Y. Ye, L. Pan, K. Koumoto, R. Zhang, C. Wan and Y. Wang, *Sci. Rep.*, 2016, **6**, 32501.

43 M. L. Liu, F. Q. Huang, L. D. Chen and I. W. Chen, *Appl. Phys. Lett.*, 2009, **94**, 202103.

44 H. Yang, L. A. Jauregui, G. Zhang, Y. P. Chen and Y. Wu, *Nano Lett.*, 2012, **12**, 540–545.

45 H. Xie, X. Su, S. Hao, C. Zhang, Z. Zhang, W. Liu, Y. Yan, C. Wolverton, X. Tang and M. G. Kanatzidis, *J. Am. Chem. Soc.*, 2019, **141**, 18900–18909.

46 Y. Zhang, L. Xi, Y. Wang, J. Zhang, P. Zhang and W. Zhang, *Comput. Mater. Sci.*, 2015, **108**, 239–249.

47 R. Zhang, K. Chen, B. Du and M. J. Reece, *J. Mater. Chem. A*, 2017, **5**, 5013–5019.

48 A. E. Becquerel, *Ann. Chim. Phys.*, 1866, **48**, 389–436.

49 W.-D. Liu, L. Yang, Z.-G. Chen and J. Zou, *Adv. Mater.*, 2020, **32**, 1905703.

50 G. Dennler, R. Chmielowski, S. Jacob, F. Capet, P. Roussel, S. Zastrow, K. Nielsch, I. Opahle and G. K. H. H. Madsen, *Adv. Energy Mater.*, 2014, **4**, 1301581.

51 J. Heo, R. Ravichandran, C. F. Reidy, J. Tate, J. F. Wager and D. A. Keszler, *Adv. Energy Mater.*, 2015, **5**, 1401506.

52 D. S. Prem Kumar, M. Ren, T. Osipowicz, R. C. Mallik and P. Malar, *Sol. Energy*, 2018, **174**, 422–430.

53 Y. Xiao, S. H. Lee and Y.-K. Sun, *Adv. Energy Mater.*, 2017, **7**, 1601329.

54 C.-H. Lai, M.-Y. Lu and L.-J. Chen, *J. Mater. Chem.*, 2012, **22**, 19–30.

55 Y.-X. Wang, W.-H. Lai, Y.-X. Wang, S.-L. Chou, X. Ai, H. Yang and Y. Cao, *Angew. Chemie Int. Ed.*, 2019, **58**, 18324–18337.

56 H. Tan, Y. Feng, X. Rui, Y. Yu and S. Huang, *Small Methods*, 2020, **4**, 1900563.

57 X. Ou, L. Cao, X. Liang, F. Zheng, H.-S. Zheng, X. Yang, J.-H. Wang, C. Yang and M. Liu, *ACS Nano*, 2019, **13**, 3666–3676.

58 M. Nakamura, K. Yamaguchi, Y. Kimoto, Y. Yasaki, T. Kato and H. Sugimoto, *IEEE J. Photovoltaics*, 2019, **9**, 1863–1867.

59 L. Zheng, F. Teng, X. Ye, H. Zheng and X. Fang, *Adv. Energy Mater.*, 2020, **10**, 1902355.

60 M. S. Faber, M. A. Lukowski, Q. Ding, N. S. Kaiser and S. Jin, *J. Phys. Chem. C*, 2014, **118**, 21347–21356.

61 S. Anantharaj, S. R. Ede, K. Sakthikumar, K. Karthick, S. Mishra and S. Kundu, *ACS Catal.*, 2016, **6**, 8069–8097.

62 S. Goel, F. Chen and W. Cai, *Small*, 2014, **10**, 631–645.

63 J. Sheng, L. Wang, Y. Han, W. Chen, H. Liu, M. Zhang, L. Deng and Y.-N. Liu, *Small*, 2018, **14**, 1702529.

64 M. D. Regulacio, Y. Wang, Z. W. Seh and M.-Y. Han, *ACS Appl. Nano Mater.*, 2018, **1**, 3042–3062.

65 P. G. Spry, S. Merlino, Su Wang, Xiaomao Zhang and P. R. Buseck, *Am. Mineral.*, 1994, **79**, 750–762.

66 A. Repstock, P. Voudouris and U. Kolitsch, *Neues Jahrb. fur Mineral. Abhandlungen*, 2015, **192**, 135–149.

67 P. Orlandi, S. Merlino, G. Duchi and G. Vezzalini, *Can. Mineral.*, 1981, **19**, 423–427.

68 G. N. Pshenichnyy, T. N. Shaldun, L. N. Vyal'sov and A. I. Tsepin, *Dokl. Acad. Sci. USSR, Earth Sci. Sect.*, 1975, **221**, 140–143.

69 E. M. Spiridonov, T. N. Chvileva and A. S. Badalov, *Int. Geol. Rev.*, 1984, **26**, 534–539.

70 F. Melcher, T. Oberthür and D. Rammlmair, *Ore Geol. Rev.*, 2006, **28**, 32–56.

71 K. Komuro and Y. Kajiwara, *Resour. Geol.*, 2004, **54**, 447–452.

72 T. Wagner and T. Monecke, *Can. Mineral.*, 2005, **43**, 655–669.

73 L. Cvetković, A. Pačevski and T. Tončić, *Geol. Ore Depos.*, 2013, **55**, 298–304.

74 L. Wenyuan, N. J. Cook, C. L. Ciobanu, L. Yu, Q. Xiaoping and C. Yuchuan, *Ore Geol. Rev.*, 2016, **72**, 682–698.

75 R. E. Landon and A. H. Mogilnor, *Am. Mineral.*, 1933, **18**, 528–533.

76 V. A. Kovalenker, T. L. Evstigneeva, V. S. Malov, N. V Trubkin, A. I. Gorshkov and V. R. Geinke, *Mineral. Zhurnal*, 1984, **6**, 88–96.

77 O. V Frank-Kamenetskaya, I. V Rozhdestvenskaya and L. A. Yanulova, *J. Struct. Chem.*, 2002, **43**, 89–100.

78 V. Pavan Kumar, A. R. Supka, P. Lemoine, O. I. Lebedev, B. Raveau, K. Suekuni, V. Nassif, R. Al Rahal Al Orabi, M. Fornari and E. Guilmeau, *Adv. Energy Mater.*, 2019, **9**, 1803249.

79 R. Shannon, *Acta Crystallogr. Sect. A*, 1976, **32**, 751–767.

80 V. Pavan Kumar, G. Guélou, P. Lemoine, B. Raveau, A. Supka, R. Al Rahal Al Orabi, M. Fornari, K. Suekuni and E. Guilmeau, *Angew. Chemie Int. Ed.*, 2019, **58**, 15455–15463.

81 C. Vaju, J. Martial, E. Janod, B. Corraze, V. Fernandez and L. Cario, *Chem. Mater.*, 2008, **20**, 2382–2387.

82 K. Peters, E.-M. Peters, H. G. von Schnering, C. Mujica, G. Carvajal and J. Llanos, *Zeitschrift für Krist. - Cryst. Mater.*, **211**, 812.

83 W. P. Binnie, M. J. Redman and W. J. Mallio, *Inorg. Chem.*, 1970, **9**, 1449–1452.

84 E. A. Pruss, B. S. Snyder and A. M. Stacy, *Angew. Chemie Int. Ed. English*, 1993, **32**, 256–257.

85 K. Suekuni, F. S. Kim and T. Takabatake, *J. Appl. Phys.*, 2014, **116**, 063706.

86 C. Bourgès, M. Gilmas, P. Lemoine, N. E. Mordvinova, O. I. Lebedev, E. Hug, V. Nassif, B. Malaman, R. Daou and E. Guilmeau, *J. Mater. Chem. C*, 2016, **4**, 7455–7463.

87 F. S. Kim, K. Suekuni, H. Nishiate, M. Ohta, H. I. Tanaka and T. Takabatake, *J. Appl. Phys.*, 2016, **119**, 175105.

88 K. Suekuni, F. S. Kim, H. Nishiate, M. Ohta, H. I. Tanaka and T. Takabatake, *Appl. Phys. Lett.*, 2014, **105**, 132107.

89 C. Bourgès, Y. Bouyrie, A. R. Supka, R. Al Rahal Al Orabi, P. Lemoine, O. I. Lebedev, M. Ohta, K. Suekuni, V. Nassif, V. Hardy, R. Daou, Y. Miyazaki, M. Fornari and E. Guilmeau, *J. Am. Chem. Soc.*, 2018, **140**, 2186–2195.

90 E. Makovicky and B. J. Skinner, *Can. Mineral.*, 1978, **16**, 611–623.

91 P. Vaqueiro, G. Guélou, A. Kaltzoglou, R. I. R. I. Smith, T. Barbier, E. Guilmeau and A. V. A. V.

Powell, *Chem. Mater.*, 2017, **29**, 4080–4090.

92 Y. Kikuchi, Y. Bouyrie, M. Ohta, K. Suekuni, M. Aihara and T. Takabatake, *J. Mater. Chem. A*, 2016, **4**, 15207–15214.

93 G. Guélou, C. Couder, A. Bourhim, O. I. Lebedev, N. Daneu, F. Appert, J. Juraszek, P. Lemoine, L. Segreto and E. Guilmeau, *Acta Mater.*, 2020, **195**, 229–239.

94 K. Suekuni, H. I. Tanaka, F. S. Kim, K. Umeo and T. Takabatake, *J. Phys. Soc. Japan*, 2015, **84**, 103601.

95 H. WYERS, *Br. J. Ind. Med.*, 1946, **3**, 177–182.

96 J. L. Domingo, *Reprod. Toxicol.*, 1996, **10**, 175–182.

97 Y. Bouyrie, M. Ohta, K. Suekuni, Y. Kikuchi, P. Jood, A. Yamamoto and T. Takabatake, *J. Mater. Chem. C*, 2017, **5**, 4174–4184.

98 P. Lemoine, C. Bourgès, T. Barbier, V. Nassif, S. Cordier and E. Guilmeau, *J. Solid State Chem.*, 2017, **247**, 83–89.

99 K. Suekuni, Y. Shimizu, E. Nishibori, H. Kasai, H. Saito, D. Yoshimoto, K. Hashikuni, Y. Bouyrie, R. Chetty, M. Ohta, E. Guilmeau, T. Takabatake, K. Watanabe and M. Ohtaki, *J. Mater. Chem. A*, 2019, **7**, 228–235.

100 Y. Bouyrie, M. Ohta, K. Suekuni, P. Jood and T. Takabatake, *J. Alloys Compd.*, 2018, **735**, 1838–1845.

101 G. Guélou, V. Pavan Kumar, A. Bourhim, P. Lemoine, B. Raveau, A. Supka, O. I. Lebedev, R. Al Rahal Al Orabi, M. Fornari, K. Suekuni and E. Guilmeau, *ACS Appl. Energy Mater.*, 2020, **3**, 4180–4185.

102 Y. Bouyrie, V. Ohorodniichuk, S. Sassi, P. Masschelein, A. Dauscher, C. Candolfi and B. Lenoir, *J. Electron. Mater.*, 2017, **46**, 2684–2690.

103 C. Candolfi, G. Guélou, C. Bourgès, A. R. Supka, R. Al Rahal Al Orabi, M. Fornari, B. Malaman, G. Le Caër, P. Lemoine, V. Hardy, J.-M. Zanotti, R. Chetty, M. Ohta, K. Suekuni and E. Guilmeau, *Phys. Rev. Mater.*, 2020, **4**, 25404.

104 Y. Pei, X. Shi, A. Lalonde, H. Wang, L. Chen and G. J. Snyder, *Nature*, 2011, **473**, 66–69.

105 M. Ochi, H. Mori, D. Kato, H. Usui and K. Kuroki, *Phys. Rev. Mater.*, 2018, **2**, 85401.

106 B. Raveau, *J. Supercond. Nov. Magn.*, 2019, **33**, 259–263.

107 L. Xi, Y. B. Zhang, X. Y. Shi, J. Yang, X. Shi, L. D. Chen, W. Zhang, J. Yang and D. J. Singh, *Phys. Rev. B*, 2012, **86**, 155201.

108 Y. Zhang, X. Yuan, X. Sun, B.-C. C. Shih, P. Zhang and W. Zhang, *Phys. Rev. B*, 2011, **84**, 75127.

109 X. Shen, Y. Xia, C. C. Yang, Z. Zhang, S. Li, Y. H. Tung, A. Benton, X. Zhang, X. Lu, G. Wang, J. He and X. Zhou, *Adv. Funct. Mater.*, 2020, **2000526**, 1–10.

110 P. Vaqueiro, R. A. R. Al Orabi, S. D. N. Luu, G. Guélou, A. V. Powell, R. I. Smith, J.-P. Song, D. Wee and M. Fornari, *Phys. Chem. Chem. Phys.*, 2015, **17**, 31735–31740.

111 C. Bourgès, P. Lemoine, O. I. Lebedev, R. Daou, V. Hardy, B. Malaman and E. Guilmeau, *Acta Mater.*, 2015, **97**, 180–190.

112 I. T. Witting, T. C. Chasapis, F. Ricci, M. Peters, N. A. Heinz, G. Hautier and G. J. Snyder, *Adv. Electron. Mater.*, 2019, **5**, 1800904.

113 G. Tan, S. Hao, J. Zhao, C. Wolverton and M. G. Kanatzidis, *J. Am. Chem. Soc.*, 2017, **139**, 6467–6473.

114 H. Lin, G. Tan, J.-N. Shen, S. Hao, L.-M. Wu, N. Calta, C. Malliakas, S. Wang, C. Uher, C. Wolverton and M. G. Kanatzidis, *Angew. Chemie Int. Ed.*, 2016, **55**, 11431–11436.

115 P. Lemoine, V. Pavan Kumar, G. Guélou, V. Nassif, B. Raveau and E. Guilmeau, *Chem. Mater.*, 2020, **32**, 830–840.

116 Y. Bouyrie, R. Chetty, K. Suekuni, N. Saitou, P. Jood, N. Yoshizawa, T. Takabatake and M. Ohta, *J. Mater. Chem. C*, 2020, **8**, 6442–6449.

117 D. Narducci, *Appl. Phys. Lett.*, 2011, **99**, 102104.

118 D. C. Cahill, S. K. Watson and R. O. Pohl, *Phys. Rev. B*, 1992, **46**, 6131–6140.

119 L. M. Rodriguez-Martinez and J. P. Attfield, *Phys. Rev. B*, 1996, **54**, 622–625.

120 P. Baláž, M. Baláž, M. Achimovičová, Z. Bujňáková and E. Dutková, *J. Mater. Sci.*, 2017, **52**, 11851–11890.

121 M. Hegedüs, M. Achimovičová, H. Hui, G. Guélou, P. Lemoine, I. Fourati, J. Juraszek, B. Malaman, P. Baláž and E. Guilmeau, *Dalt. Trans.*, 2020, **49**, 15828–15836.

122 R. Chetty, Y. Kikuchi, Y. Bouyrie, K. Suekuni, A. Yamamoto, P. Jood and M. Ohta, *J. Mater. Chem. C*, 2019, **7**, 5184–5192.

123 Y. M. Han, J. Zhao, M. Zhou, X. X. Jiang, H. Q. Leng and L. F. Li, *J. Mater. Chem. A*, 2015, **3**, 4555–4559.

124 J.-B. Labégorre, A. Virfeu, A. Bourhim, H. Willeman, T. Barbier, F. Appert, J. Juraszek, B. Malaman, A. Huguenot, R. Gautier, V. Nassif, P. Lemoine, C. Prestipino, E. Elkaim, L. Pautrot-d'Alençon, T. Le Mercier, A. Maignan, R. Al Rahal Al Orabi and E. Guilmeau, *Adv. Funct. Mater.*, 2019, **9**, 1904112.

125 P. Mangelis, P. Vaqueiro and A. V. Powell, *ACS Appl. Energy Mater.*, 2020, **3**, 2168–2174.

126 M. Ohta, H. Obara and A. Yamamoto, *Mater. Trans.*, 2009, **50**, 2129–2133.

127 R. Chmielowski, S. Bhattacharya, W. Xie, D. Péré, S. Jacob, R. Stern, K. Moriya, A. Weidenkaff, G. K. H. H. Madsen and G. Dennler, *J. Mater. Chem. C*, 2016, **4**, 3094–3100.

128 M. Beaumale, T. Barbier, Y. Bréard, G. Guelou, A. V. Powell, P. Vaqueiro and E. Guilmeau, *Acta Mater.*, 2014, **78**, 86–92.

129 T. Tanimoto, K. Suekuni, T. Tanishita, H. Usui, T. Tadano, T. Kamei, H. Saito, H. Nishiate, C. H. Lee, K. Kuroki and M. Ohtaki, *Adv. Funct. Mater.*, 2020, **30**, 2000973.

130 P. Baláž, M. Hegedüs, M. Reece, R.-Z. Zhang, T. Su, I. Škorvánek, J. Briančin, M. Baláž, M. Mihálik, M. Tešínsky and M. Achimovičová, *J. Electron. Mater.*, 2019, **48**, 1846–1856.

131 K. Biswas, L.-D. Zhao and M. G. Kanatzidis, *Adv. Energy Mater.*, 2012, **2**, 634–638.

132 B. Du, R. Zhang, M. Liu, K. Chen, H. Zhang and M. J. Reece, *J. Mater. Chem. C*, 2019, **7**, 394–404.

133 S. O. J. Long, A. V Powell, P. Vaqueiro and S. Hull, *Chem. Mater.*, 2018, **30**, 456–464.

134 L. D. Zhao, S. H. Lo, J. He, H. Li, K. Biswas, J. Androulakis, C. I. Wu, T. P. Hogan, D. Y. Chung, V. P. Dravid and M. G. Kanatzidis, *J. Am. Chem. Soc.*, 2011, **133**, 20476–20487.

135 L. D. Zhao, J. He, S. Hao, C. I. Wu, T. P. Hogan, C. Wolverton, V. P. Dravid and M. G. Kanatzidis, *J. Am. Chem. Soc.*, 2012, **134**, 16327–16336.

136 X. Lu and D. T. Morelli, *Phys. Chem. Chem. Phys.*, 2013, **15**, 5762–5766.